Titre: Title:	New Circular Polarization Selective Surface Concepts Based on The Pierrot Cell Using Printed Circuit Technology
Auteur: Author:	Humberto Israel Lopez
Date:	2013
Type:	Mémoire ou thèse / Dissertation or Thesis
Référence: Citation:	Lopez, H. I. (2013). New Circular Polarization Selective Surface Concepts Based on The Pierrot Cell Using Printed Circuit Technology [Mémoire de maîtrise, École Polytechnique de Montréal]. PolyPublie. https://publications.polymtl.ca/1299/

URL de PolyPublie: PolyPublie URL:	https://publications.polymtl.ca/1299/
Directeurs de recherche: Advisors:	Jean-Jacques Laurin
Programme: Program:	génie électrique

UNIVERSITÉ DE MONTRÉAL

NEW CIRCULAR POLARIZATION SELECTIVE SURFACE CONCEPTS BASED ON THE PIERROT CELL USING PRINTED CIRCUIT TECHNOLOGY

HUMBERTO ISRAEL LOPEZ
DÉPARTEMENT DE GÉNIE ÉLECTRIQUE
ÉCOLE POLYTECHNIQUE DE MONTRÉAL

MÉMOIRE PRÉSENTÉ EN VUE DE L'OBTENTION
DU DIPLÔME DE MAÎTRISE ÈS SCIENCES APPLIQUÉES
(GÉNIE ÉLECTRIQUE)
NOVEMBRE 2013

UNIVERSITÉ DE MONTRÉAL

ÉCOLE POLYTECHNIQUE DE MONTRÉAL

Ce mémoire intitulé :

NEW CIRCULAR POLARIZATION SELECTIVE SURFACE CONCEPTS BASED ON THE PIERROT CELL USING PRINTED CIRCUIT TECHNOLOGY

présenté par : LOPEZ, Humberto Israel
en vue de l'obtention du diplôme de : Maîtrise ès sciences appliquées
a été dûment accepté par le jury d'examen constitué de :

M. AKYEL Cevdet, D.Sc.A., président
M. LAURIN Jean-Jacques, Ph.D., membre et directeur de recherche
M. WU Ke, Ph.D., membre

To my lovely wife,

ACKNOWLEDGMENTS

First of all I would like to express my sincere gratitude to my research director, Professor Jean-Jacques Laurin for all his support, patience and guidance throughout this project. He was always there when I needed advise. I consider myself fortunate to been able to work under his supervision. He is a great influence in my career. I would not be in this field of study if it was not for him.

I would like to thank as well professors Cevdet Akyel and Ke Wu for serving on my thesis committee. Their vast knowledge and experience helped me in many ways during my studies.

A special thank goes to the technical staff at Poly-Grames, Steve Dubé, Traian Antonescu and Maxime Thibault for their hard work and advice for the fabrication and measure of the prototypes built for this project. Their patience is also very much appreciated. Also, I would like to thank Jean-Sébastien Décarie for his efficient support whenever I needed it.

I extend my gratitude also to my fellow students at Poly-Grames, especially to Marc-André Joyal for all his support and advice for the development of this project.

Furthermore, I would like to thank Nathalie Lévesque and Ginette Desparois for their friendly and helpful service.

Finally, I extend my gratitude to my wife Indira Vaca. Without her patience, encouragement and support I would not be where I am right now.

RÉSUMÉ

Ce mémoire porte sur la recherche d'une méthode alternative permettant de construire une surface sélective en polarisation circulaire (circular polarization selective surface, ou CPSS) basée sur la cellule de Pierrot en utilisant la technologie des circuits imprimés. Cette technique de fabrication utilise un substrat mince plié, ce qui permet la mise en œuvre des cellules de Pierrot sur une couche de métal définie par des techniques de circuits imprimés de précision, sans avoir besoin de trous d'interconnexion métallisés. Différentes topologies des CPSS sont analysées afin de rendre le CPSS plus efficace en termes de bande passante et de l'indépendance de l'angle d'arrivée de l'onde incidente. Des prototypes de CPSS réfléchissants pour la polarisation circulaire gauche et transparents pour la polarisation circulaire droite sont conçus pour illustrer les avantages de l'approche proposée.

Le premier prototype est un CPSS composé de cellules simples de Pierrot optimisées pour avoir de bons coefficients de réflexion et de transmission. Ce prototype a été construit et ensuite caractérisé par un banc de test en fonctionnement dans la bande K. Les coefficients de transmission des ondes planes en incidence normale et de polarsations circulaires droite et gauche sont -0.48 dB et -24 dB respectivement. La bande passante obtenue pour un coefficient de transmission de la polarisation circulaire gauche inférieure à -3 dB était de 17.6%. Ces résultats sont en bon accord avec les résultats de simulations obtenus avec HFSS.

Une deuxième variante considérée est une cellule de Pierrot avec une charge série ajoutée sur le segment du milieu. Grâce à cette cellule, il est possible d'égaliser les fréquences pour lesquelles il y a un meilleur fonctionnement pour les polarisations circulaires droite et gauche. Cette cellule a permis d'obtenir une amélioration pour le rapport copolarisation à polarisation croisée pour les ondes RHCP de 10 dB à 20 GHz. La charge supplémentaire n'affecte pas la performance de la polarisation circulaire gauche comme prévu.

La troisième variante est une cellule de Pierrot à 90 degrés. Cette cellule est conçue afin de permettre d'imprimer sur le même substrat deux types de cellules fonctionnant à des fréquences différentes, et ainsi permettre d'élargir la bande de fonctionnement des CPSS. Malheureusement, le rapport axial pour cette configuration est beaucoup détérioré, tandis que le reste des résultats demeure à de bonnes valeurs.

Une quatrième alternative étudiée dans ce mémoire est la double cellule de Pierrot. Cette configuration permet au CPSS d'avoir des performances qui sont moins dépendantes de l'angle d'arrivée des ondes incidentes. De plus, en réglant la densité de cellules, on obtient une meilleure performance. Un prototype a été construit et caractérisé. Une augmentation de la bande passante à 40% a été observée. Une composition de deux cellules fonctionnant à

des fréquences différentes est analysée aussi. Cependant, alors que la bande passante reste acceptable, le rapport axial et la performance globale à des fréquences plus élevées sont détériorés.

Une dernière étude a porté sur les pertes introduites par le support en mousse utilisé dans la fabrication des CPSS. En raison de la valeur élevée du facteur de dissipation, le support contribue de façon importante aux pertes du système. En diminuant la densité de la mousse, il est possible de réduire les pertes, d'où l'incrémentation des performances. Un prototype avec trous rectangulaires sur le support de mousse a été fabriqué à fin de prouver cette fait. Cette configuration a permis d'augmenter le coefficient de transmission du CPSS pour une onde incidente en polarisation circulaire droite de 0.4 dB (-0.5 dB à -0.1 dB) à 20 GHz.

En conclusion, comparativement à d'autres modèles de CPSS basées sur la cellule de Pierrot présentés dans la littérature, la nouvelle méthode de fabrication proposée dans ce mémoire simplifie le processus de fabrication tout en donnant une performance meilleure ou similaire. Il est également montré que le processus de fabrication utilisé donne plus de liberté au concepteur en permettant d'ajuster les cellules pour augmenter les performances et la bande passante du CPSS.

ABSTRACT

This M.A.Sc. thesis focuses on finding an alternative method of constructing a circular polarization selective surface (CPSS) based on the Pierrot cell using the standard printed circuit technology. This technique uses a folded flexible substrate, which enables the implementation of the 3D Pierrot cells on a single metal layer defined with precision printed circuit board techniques, without the need for metalized via holes. Different topologies of the CPSS are analyzed in order to make the CPSS more efficient in terms of bandwidth and independence on the direction of propagation of the incident wave. A left-hand CPSS is designed to illustrate the benefits of the proposed approach.

The first approach is a simple Pierrot unit cell CPSS which is optimized to have good reflection and transmission coefficients. A prototype is built and then characterized in a test bench operating in the K-band. For the fabricated prototype, the transmission coefficients of plane waves at normal incidence in the right-hand and the left-hand circular polarizations are -0.48 dB and -24 dB respectively. The bandwidth for which the transmission coefficient of the incident left-handed incident wave is greater than -3 dB was of 17.6%. These results are in good agreement with simulations results obtained with HFSS.

A second variant considered is a Pierrot cell with a series load in the middle segment. With this cell it is possible to equalize the frequencies giving a better operation in the right- and left-handed circular polarized waves. There is an improvement for the co-pol to cross-pol ratio for the RHCP waves of 10 dB at 20 GHz. The added load does not affect the performance for the left-hand circular polarization, as expected.

The third modification is a Pierrot cell at 90 degrees. This cell is designed to allow the combination of two Pierrot cells working at different frequencies on the same substrate in order to increase the frequency bandwidth of the CPSS. Unfortunately, the axial ratio for this configuration is much deteriorated while the rest of the results remain at good values.

A fourth alternative is the double Pierrot cell. This configuration allows the CPSS to have more independence on the angle of the incident waves. Also, by adjusting the cell density, a better performance is obtained. A prototype was built and characterized and it showed an increase in bandwidth of 40%. A combination of two cells operating at different frequencies was analyzed as well. However, while the bandwidth increased slightly, the axial ratio and overall performance at higher frequencies was deteriorated.

Finally, a study was made on the losses introduced by the foam layers supporting the PCB. Because of the high value of the foam loss tangent, the support introduces an important amount of losses to the system. By lowering its density it is possible to reduced losses, hence

incrementing the performances. A prototype with rectangular holes was fabricated to prove this statement, increasing the RHCP transmission coefficient by 0.4 dB (-0.5 dB to -0.1 dB) at 20 GHz.

In conclusion, this thesis shows that compared to other Pierrot cell designs presented in the literature, the new approach simplifies the fabrication process while giving better or similar performance. It is also shown that the fabrication process proposed gives more freedom by allowing the designer to adjust the cells to increase the performance and the bandwidth of the CPSS.

CONDENSÉ EN FRANÇAIS

Le but du projet de recherche décrit dans ce mémoire est de proposer une méthode alternative pour la fabrication d'une Surface Sélective en Polarisation Circulaire (on utilisera l'acronyme anglais CPSS pour Circular Polarisation Selective Surface) basée sur la cellule de Pierrot en utilisant les technologies de circuit imprimé standard. En tirant profit des nouveaux degrés de liberté pour la fabrication du CPSS permis par la méthode de fabrication proposée, nous étudions aussi une série de modifications à la cellule de Pierrot afin d'améliorer la largueur de bande et rendre la structure moins dépendante de la direction de propagation des ondes incidentes.

Ce mémoire s'articule autour de quatre chapitres. Le premier chapitre présente une brève introduction de fonctionnement des CPSS, suivi d'une revue de littérature décrivant les différentes mises en œuvres des cellules de Pierrot. Le deuxième chapitre porte sur la nouvelle méthode de fabrication d'un CPSS sur un substrat mince flexible avec les technologies de circuit imprimé standard. Le troisième chapitre est consacré à l'étude de quelques variations de la cellule de Pierrot visant à améliorer la performance des CPSS. Une des modifications considérées consiste à ajouter une charge sur le segment central, tant que le reste de modifications sera de diverses configurations de la cellule double de Pierrot. Finalement, nous ferons une analyse du support de mousse utilisée en ses CPSS. Le dernier chapitre conclut ce mémoire et présente des avenues possibles de travaux futurs.

Chapitre 1 : Introduction

Le poids et le volume des antennes sont toujours des éléments clés dans la conception des charges utiles des satellites de communications. Pour avoir une meilleure utilisation du spectre de fréquence, les opérateurs utilisent souvent des polarisations orthogonales sur une même plage de fréquence. En polarisation linéaire, ceci est réalisé couramment avec des réflecteurs à double grille consistant en deux réflecteurs paraboliques superposés, chacun fonctionnant dans une polarisation linéaire orthogonale à celle de l'autre réflecteur. Jusqu'à présent il n'a pas été possible de mettre en œuvre un système de réflecteurs superposés fonctionnant avec des polarisations circulaires orthogonales. Par contre, la polarisation circulaire est en grande demande pour les futurs satellites de communications à large bande en bandes K et Ka. Une alternative pour attaquer cette problématique est d'utiliser un double réflecteur fait avec deux CPSS.

Dans ce mémoire, nous utiliserons un CPSS de type main gauche (LHCPSS) pour illustrer leur comportement et faire le design. Par analogie, une CPSS de main droite (RHCPSS)

peut être construite assez facilement. Un LHCPSS réfléchit les ondes en polarisation circulaire gauche (LHCP) et il est transparent pour les ondes en polarisation circulaire droite (RHCP). Avec une structure périodique construite à base de cellules de Pierrot, il est possible de construire un CPSS.

Chapitre 2 : Une nouvelle méthode pour le design et fabrication d'un CPSS basée sur la cellule de Pierrot

Ce chapitre commence par le développement des équations nécessaires pour étudier les CPSS. Nous utilisons les ports de Floquet pour l'analyse. La première analyse a été faite sur un réseau de cellules de Pierrot dans l'espace libre. La cellule a été optimisée en changeant les longueurs de segments et le largueur du ruban métallique pour maximiser la transmission des ondes RHCP et la réflexion des ondes LHCP. Les coefficients de transmission sur illumination RHCP et de réflexion sur illumination LHCP sont de 0 dB. Les rapports axiaux (AR) de transmission et réflexion ont une valeur de 0.01 dB à 20 GHz.

La prochaine étape est l'ajout du soutien à la structure. La solution originale présentée dans ce mémoire consiste à mettre en œuvre le CPSS sur un substrat flexible très mince pliable avec un support de mousse. Le substrat choisi est le Pyralux AP 8525R de Dupont d'épaisseur de 2 mils. Ce substrat est facilement pliable et ses pertes sont assez faibles. Nous avons évalué trois types de mousse d'Evonik pour trouver celle qui s'adapte mieux aux besoins. La mousse choisie a été le Rohacell 31 HF qui donne les meilleurs résultats du point de vue de pertes. Pour trouver la densité de cellules appropriée, nous avons évalué trois périodes de cellules, 8.5 mm $\times$ 8.5 mm, 9 mm $\times$ 9 mm and 10 mm $\times$ 10 mm. Chaque cellule a été optimisée avec la procédure indiquée précédemment. La meilleure était celle de 10 mm $\times$ 10 mm qui a mené à un bon compromis dans les réponses en fréquence du CPSS.

Nous avons choisi cette dernière cellule pour fabrication. Le circuit imprimé est muni de trous sur les côtés droit et gauche. Ces trous sont utilisés pour plier le substrat avec l'outil fabriqué spécialement pour cette tâche. Après le pliage, quatre circuits ont été coupés et placés sur un morceau de mousse machiné avec un profil crénelé. Un deuxième morceau de mousse a été placé sur la structure comme dernière étape dans lassemblage. Avec cette méthode, nous n'utilisons pas d'adhésif et la procédure reste assez simple. Pour caractériser ce prototype, un banc de test en espace libre a été utilisé. À 20 GHz, les valeurs mesurées des coefficients de transmission RHCP et LHCP sont de -20.7 dB et -0.5 dB respectivement. Les simulations donnent des valeurs de -24 dB et -0.5 dB. La larguer de bande en transmission est de 27% et 17.6% pour la simulation et les mesures respectivement. La larguer de bande du rapport axial inférieur à 1 dB de l'onde transmise en polarisation droite est de 19.83-22.54 GHz pour les mesures, pour la simulation elle est de 18.49-21.26 GHz.

Chapitre 3 : Amélioration de performances du CPSS imprimé

La première variation étudiée est la cellule de Pierrot avec une charge série sur le segment centrale. Cette modification à la cellule vise à avoir de meilleures performances de polarisation croisée. Pour une simple cellule de Pierrot, la fréquence à laquelle le minimum de polarisation croisée en réflexion est différent de la fréquence du minimum de polarisation croisé en transmission. Le minimum de transmission de polarisation croisée pour les ondes LHCP de -28 dB est à 20 GHz alors que pour les ondes RHCP le minimum de -45 dB est à 22.2 GHz. Le fait que pour illumination LHCP la distribution de courant induit sur la cellule de Pierrot a un nul sur le centre permet d'ajouter une charge sans perturber le comportement pour les ondes en polarisation circulaire gauche. Par contre, pour les ondes en polarisation circulaire droite, cela permet de réduire le courant à la fréquence de design. La période de la cellule reste la même, 10 mm $\times$ 10 mm. La cellule a été optimisée pour maximiser la transmission des ondes RHCP et la réflexion des ondes LHCP et minimiser la transmission des ondes LHCP et la réflexion des ondes RHCP. La réflexion minimale en illumination RHCP s'est décalée de 22.2 GHz à 19.7 GHz avec une réduction de -19 dB à -28 dB à 20 GHz. Cette fréquence est maintenant la même que la fréquence pour le minimum de transmission en illumination LHCP. Les coefficients de transmission RHCP et réflexion LHCP ont de performances similaires pour les deux cellules. Le ratio copolarisation à polarisation croisé pour les ondes RHCP pour la cellule avec charge a été amélioré de 10 dB à 20 GHz, alors que pour les ondes LHCP, la performance reste la même, comme prévu. Par contre, on a eu une légère diminution sur la largeur de bande de transmission de 27.2% à 23.3%.

Nous considérons maintenant avec l'étude de diverses variations sur la cellule de Pierrot double. La première variation de la cellule double est la cellule à 90 degrés. Le segment supérieur est imprimé sur le mur vertical à la place d'être sur la section horizontale du dessus. Ce segment forme un angle de 90 degrés avec le segment horizontal qui est aussi imprimé sur le mur. Le segment inférieur est perpendiculaire au mur vertical. Nous avons étudié la cellule seule, mais la configuration de cette cellule serait une de cellule double. Cette cellule est conçue pour fonctionner à une fréquence supérieure (22 GHz) à la fréquence de fonctionnement de la cellule originale qui avait été conçue pour 20 GHz. La période de la cellule à 90 degrés est 10 mm $\times$ 10 mm et elle est optimisée comme dans les autres cas. Sur illumination RHCP, les coefficients de transmission ont une valeur de -0.5 dB pour les deux cellules ; et la réflexion a une valeur de -30 dB. Nous constatons que la largeur de bande en transmission est tombée considérablement de 27% à 12%. Aussi, le rapport axial est très détérioré. L'étude de cette cellule n'a pas été poussée plus loin, car il n'y a pas une amélioration de performance satisfaisante.

Une autre cellule double qui a été proposée est la cellule à double Pierrot. Cette cellule a une symétrie de rotation d'ordre 2, ce qui permet de réduire la dépendance à l'angle d'arrivée. Ce modèle consiste à avoir deux cellules de Pierrot identiques avec une rotation entre elles de 180 dégréés par rapport à l'axe z. La période de la cellule est aussi de 10 mm $\times$ 10 mm comme dans les autres cellules et les longueurs et la largueur de segment a été optimisée comme pour la cellule simple. La largueur de bande a diminué de 27% de la cellule simple à 23% de la double. Par contre, la cellule double a un léger avantage pour le coefficient de réflexion en illumination LHCP de -0.65 dB contre -0.96 dB de la cellule simple. La réponse fréquentielle du coefficient de transmission en illumination RHCP est le même pour les deux cas, -0.35 dB. Le coefficient de réflexion en illumination RHCP est beaucoup plus centré sur la fréquence de design. Nous avons fait une comparaison des coefficients de transmission en illumination LHCP en fonction de l'angle d'incidence θ dans les planes ϕ=45, 22.5 et 0 degré à 20 GHz. Nous observons que les performances de la cellule simple se détériorent plus rapides que celles de la cellule double.

Pour améliorer encore plus les performances de la cellule double, nous avons évalué trois autres périodes de cellules (5 mm $\times$ 10 mm, 6 mm $\times$ 9 mm, 7 mm $\times$ 11 mm, 10 mm $\times$ 10 mm) pour améliorer leur densité et avoir une meilleure réponse fréquentielle. Chaque cellule a été optimisée avec le même critère que précédemment. Nous avons fait une comparaison des coefficients de transmission en illumination LHCP pour ces cellules. Nous observons que la cellule avec la période de 7 mm $\times$ 11 mm a les meilleurs résultats pour la largueur de bande de transmission (40%) et un coefficient de transmission minimal à 20 GHz de -28 dB. Par contre, le comportement de la cellule double avec une période de 7 mm $\times$ 11 mm est détérioré à haute fréquence. Ceci confirme qu'avec une meilleure densité de cellules, la largueur de bande est augmentée. Cette cellule donne de meilleurs résultats à la fréquence de design pour le ratio copolarisation à polarisation croisée.

La prochaine variante consiste en une cellule double, mais dont chaque élément est conçu pour une fréquence différente. La principale contrainte de cette approche est que les deux cellules partagent le mur du substrat. Cela impose que la longueur du segment vertical ne soit pas de $\lambda/4$. Une possibilité est de faire varier l'angle entre les deux segments horizontaux. De cette manière, nous raccourcissons (ou élargissons selon le cas) l'angle nécessaire pour avoir les champs tangentiels aux segments horizontaux. Nous avons testé trois fréquences (18, 19 et 21 GHz) en plus de la fréquence de design. L'angle entre les segments de la cellule à 20 GHz est toujours de 90 degrés. Premièrement, la cellule à 20 GHz a été optimisée. Avec les dimensionnes fixes, la deuxième cellule a été ajoutée et optimisée aussi en gardant toujours la longueur du segment vertical fixe. Nous constatons que les coefficients de transmission pour illumination RHCP sont autour de -0.4 dB pour les quatre cas (18-20, 19-20, 20-20 et 21-20

GHz). Par contre, les coefficients tombent après 22 GHz comme observés précédemment. Néanmoins, il y a une augmentation de la largueur de bande. Nous constatons que le rapport axial est centré sur diverses fréquences pour chaque cas. La largueur de bande est plus large, mais le prix à payer c'est une dégradation sur le rapport axial.

Pour valider le fonctionnement de la cellule à double Pierrot, nous avons fabriqué un prototype. Le prototype choisi était celui avec une période de 7 mm $\times$ 11 mm, car il a une largueur de bande importante (40%) et son ratio copolarisation à polarisation croisé a de bonnes caractéristiques à 20 GHz. Ce prototype a été caractérisé avec le même banc de test en espace libre utilisé pour la cellule simple. La cellule double a une augmentation de la larguer de bande (33% contre 17.6% de la simple). Les coefficients de transmission en illumination RHCP à 20 GHz pour les cellules simple et double sont -0.55 dB et -0.3 dB respectivement. Nous avons fait une comparaison de la variation du coefficient de transmission en illumination LHCP à 20 GHz en fonction de θ sur le plan ϕ=45 degrés pour les deux cellules en simulation et en mesures. Ces résultats confirment que la cellule double offre une meilleure indépendance à l'angle d'arrivée que la simple.

Nous discutons finalement de l'impact de la mousse sur les performances du CPSS. À la fréquence de design, les caractéristiques électriques de la mousse de Rohacell utilisée pour la fabrication pourraient être une cause importante de pertes dans le système. À fin de vérifier cette hypothèse, nous avons étudié deux modifications au support de mousse. La première était de réduire l'épaisseur la mousse à 1 mm au lieu de 5.5 mm. La deuxième était de faire trous carrés au support déjà machiné ou il y a une forte concentration des champs électriques. De cette façon, la mousse donne encore de soutien à la structure. Nous constatons que pour le coefficient de transmission en illumination RHCP il y a eu une amélioration de -0.4 dB à -0.2 dB. Pour le modèle avec trous, le coefficient de réflexion en illumination LHCP a augmenté de -0.65 dB à -0.28 dB à la fréquence de design. Nous avons fabriqué le support de mousse utilisé sur la cellule simple. Après caractérisation et à 20 GHz, le coefficient de transmission en RHCP a augmenté pour la mousse avec trous de -0.5 dB à -0.1 dB.

Chapitre 4 : Conclusions

La nouvelle technique proposée pour construire des CPSS basées sur la cellule de Pierrot donne beaucoup de liberté et permet de modifier la cellule sans difficulté. Nous avons prouvé que cette nouvelle approche donne des résultats meilleurs ou similaires à d'autres CPSS rapportés dans la littérature. Si on ajoute une charge au milieu du segment vertical, il est possible d'améliorer les performances en polarisation croisée. Nous avons constaté qu'avec une cellule double de symétrie de rotation, le CPSS devient moins dépendant aux variations de l'angle d'arrivée. Aussi pour la cellule double, avec une densité appropriée de cellules, la

largueur de bande de transmission est augmentée considérablement. Avec les cellules doubles à deux fréquences, il est possible d'augmenter encore plus la largueur de bande. Néanmoins, le prix à payer est une dégradation de coefficient de transmission en illumination RHCP à haute fréquence et aussi du rapport axial. Nous avons aussi prouvé que la mousse introduit des pertes sur le CPSS, cependant il est possible de les réduire en faisant des trous sur le support.

Pour améliorer encore plus les performances par rapport à l'angle d'arrivée, on pourrait ajouter de couches diélectriques à chaque côté du CPSS. De cette manière, en utilisant la loi de Snell, l'angle d'arrivée peut être diminué. Tous les CPSS conçus et analysés dans le cadre de ce mémoire ont un support planaire. Si on voulait installer ces CPSS sur une surface concave, comme un réflecteur parabolique, il serait nécessaire de faire une recherche approfondie sur le sujet. Une autre possibilité serait de remplacer les réflecteurs paraboliques par des réseaux réflecteurs (reflectarrays) plans. Il deviendrait alors nécessaire de mettre en œuvre une méthode permettant le contrôle de phase dans chaque cellule élémentaire du CPSS.

CONTENTS

LIST OF TABLES

LIST OF FIGURES

LIST OF APPENDICES

LIST OF ABBREVIATIONS AND NOTATIONS

AR	Axial Ratio
CP	Circular Polarization
CPSS	Circular Polarization Selective Surface
HFSS	High Frequency Structure Simulator
λ	Wavelength in free space
LHCP	Left Hand Circular Polarization
LHCPSS	Left Hand Circular Polarization Selective Surface
LP	Linear Polarization
LRM	Line-Reflect-Match
PCB	Printed Circuit Board
RHCP	Right Hand Circular Polarization

CHAPTER 1

INTRODUCTION

The weight and volume of antennas are always important factors in the design of communication satellite payloads. For doing a more efficient use of the allocated frequency spectrum, satellite operators can reuse the same frequency in two orthogonal polarizations in adjacent ground coverages. On the other hand, using two separate orthogonally polarized reflector antenna systems makes the weight and volume minimization problem more difficult. To address this issue, payload designers resort to the dual grid reflector (DGR) antenna technology.

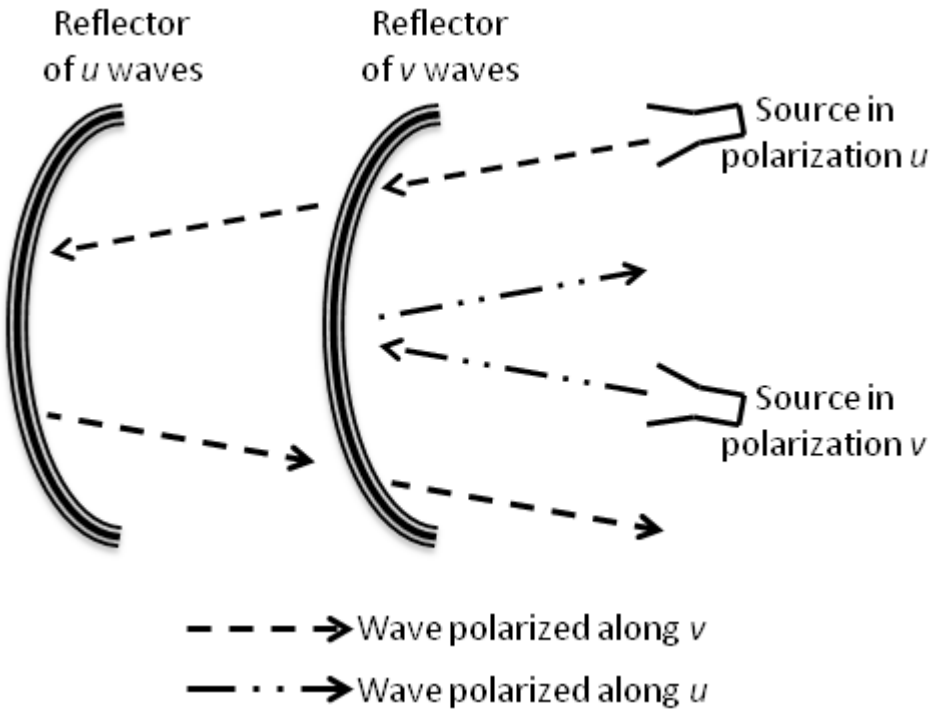

Figure 1.1: Representation of a dual grid reflector.

In a DGR system, two parabolic reflectors made of wire grids are oriented in orthogonal directions. The two reflectors are placed one behind each other (see Fig. 1.1). Let us assume a dual linear polarization feed system operating in orthogonal polarizations u and v. The first reflector is transparent to one of the linear polarizations, say u. This u polarization is then focused by the second reflector, which could either be a grid of metallic wires in the u direction or more simply a solid reflector. Waves in polarization v are however reflected by the v-oriented grid of the first reflector and they never interact with the second reflector. It

can easily be understood that the DGR arrangement has great benefits in terms of volume savings.

There are several systems that use circular polarization. The latter is especially desired for communications with mobiles because it is not necessary to ensure the alignment of the direction of the polarization of the antennas, as it is the case with linear polarization.

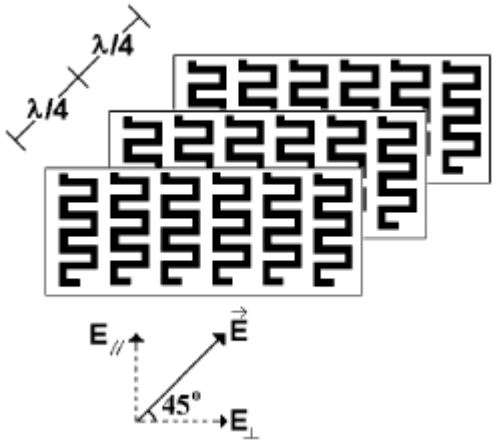

Figure 1.2: Example of a meander-line circular polarizer with three surfaces described by Joyal and Laurin (2012).

There are currently no systems with superposed reflectors (i.e. analogous to the dual-grid systems in linear polarization) operating in circular polarization. A possible approach to creating such a system described in Roy and Shafai (1996) consists of modifying a conventional dual-grid antenna by adding in front of it a polarizing surface to convert two waves with orthogonal circular polarizations to waves with orthogonal linear polarization. Fig. 1.2 shows a meander-line circular polarizer with three surfaces described by Joyal and Laurin (2012) For example, a right-hand circular polarization (RHCP) wave is converted to a horizontal polarized wave, whereas a left-hand circular polarization (LHCP) wave is converted to a vertical polarized wave. After reflection by the dual grid parabolic reflectors, the linearly polarized waves propagate once again through the circular polarizer, and as a result two circularly polarized focused beams are obtained. Such approach allows the use of existing highly efficient dual-grid reflectors. An experimental demonstration of such a system was made by Joyal *et al.* (2012) [APS2012, ICSSC2012] and good performance was obtained.

An alternative to this approach is to use a dual reflector made of Circular Polarization Selective Surfaces (CPSS). With a CPSS, polarizers converting linear polarization into circular polarization are no longer needed and the antenna structure becomes simpler. By analogy with the dual-grid systems, it is sufficient to stack a parabolic reflector made of a CPSS reflecting the right-hand circular polarization (or left-hand) with another parabolic reflector

made of a CPSS reflecting the left-hand circular polarization (or right-hand). To our knowledge, no system with stacked reflectors based on CPSS has been designed and manufactured to date. A major challenge is the realization of a CPSS that has acceptable performance, which is a sufficiently low cross-polarization, a sufficient bandwidth to accommodate broadband communications systems and independence of the polarizing properties on the angle of incidece. Several prototypes reported in the scientific literature are described in the following paragraphs. The performances obtained so far are encouraging, but improvements are needed before considering the use of CPSS in a space mission. However, the manufacturing techniques used were rudimentary. In addition, the frequencies used were limited to the C and X bands, even though the needs of current and future communication satellites are rather in bands located around 20 and 30 GHz. Achieving efficient CPSS operating at high frequencies thus remains a real problem, and it is in this vein that this work is oriented.

In the following paragraphs we explain the operating principles of a Pierrot cell CPSS followed by a brief literature review of other CPSS implementations. In the second chapter of this work, we will introduce a new process to implement a CPSS over a flexible substrate using standard printed circuit technology. We will describe the necessary steps to build a prototype operating in the K-band. In the third chapter, we will explore a few variants of the simple unit Pierrot cell CPSS to increase the performances regarding bandwidth and independence to the angle of incidence. One variant will be a simple unit Pierrot cell with a load in the middle of the vertical segment. The other variants will be double crank Pierrot cells. A comparison between the cells will be discussed in addition to a study of the effects of the foam support used in these CPSS.

1.1 Definitions and basic concepts

A left-hand CPSS (LHCPSS) completely reflects an incident left-hand circular polarized wave (LHCP) without changing its polarization. If the incident wave has right-hand circular polarization (RHCP), the LHCPSS shall transmit it without loss and without changing its polarization. A right-hand CPSS (RHCPSS) does exactly the opposite. Throughout this work, we only considered a LHCPSS. However, the results are immediately transferable to the case of RHCPSS by applying a simple geometry transformation. Figure 1.3 shows how a LHCPSS is expected to work.

One of the structures that can act as a CPSS is a periodic array of Pierrot cells (see Pierrot, 1966). The unit cell shown in Fig. 1.4 cell consists of a “crank” shaped wire made of two horizontal metal segments of $3\lambda/8$ oriented at 90 degrees with respect to each other. The two segments are connected by a vertical segment of length $\lambda/4$, whose orientation is the same

as the direction of propagation of the presumed incident wave. Here λ is the wavelength in the ambient media (i.e. air). The relative orientation of the two horizontal segments determines whether the cell will form a LHCPSS or a RHCPSS. The one in Fig. 1.4 corresponds to a LHCPSS.

To understand how the cell operates, consider an incident LHCP wave propagating in the direction $+z$. Let us assume that at the instant $t = t_0$ that the electric field points in the direction $+x$ in the plane $z = 0$. Then at the same time it will point in the direction $+y$ in the plane $z = \lambda/4$, considering the delay of a quarter cycle of the rotation of the E vector in that plane relative to the first. The two ends of the Pierrot cell, of total length λ, will therefore be excited in phase, leading to a resonance with induced high currents. To an observer in the far field on the axis $+z$, the field scattered by the segment oriented in x arrives with a delay of one quarter cycle behind the field scattered by the segment oriented in y. This due to the vertical distance (i.e. along z) of $\lambda/4$ between the two segments. This will result in a scattered LHCP wave. Because of the resonant condition of the cell, the scattered wave is in antiphase with the incident wave, and if the density of the periodic structure is adequate, the incident and the scattered waves in the $+z$ direction will cancel each other. In contrast, for an observer located on the axis $-z$, the scattered field on the segment oriented in y will arrive with a quarter of a cycle behind the scattered field oriented in x. This therefore generates a reflected LHCP wave.

If the incident wave coming towards $+z$ is of RHCP type, the segments x and y will be excited in antiphase and in these conditions the Pierrot cell of total length λ will be in antiresonance with induced currents of very low amplitude. The result is that the RHCP wave will propagate through the CPSS without attenuation or reflection.

The relatively simple geometry of the Pierrot cell suggests that the fabrication of a periodic array of cells is relatively simple. It is not the case in practice. In fact, the delay of a quarter of a cycle between the two planes of horizontal segments requires a long thin quarter-wavelength vertical segment. The length to diameter ratio is not achievable in practice according to the design rules of via holes of standard printed circuits processes. Another problem to consider is that the insulating medium mechanically supporting the Pierrot cells must have the electrical and magnetic properties of the surrounding media (e.g. air) to avoid reflections. Metallized via holes, even if they were feasible, should be made in an air substrate, which is of course impossible.

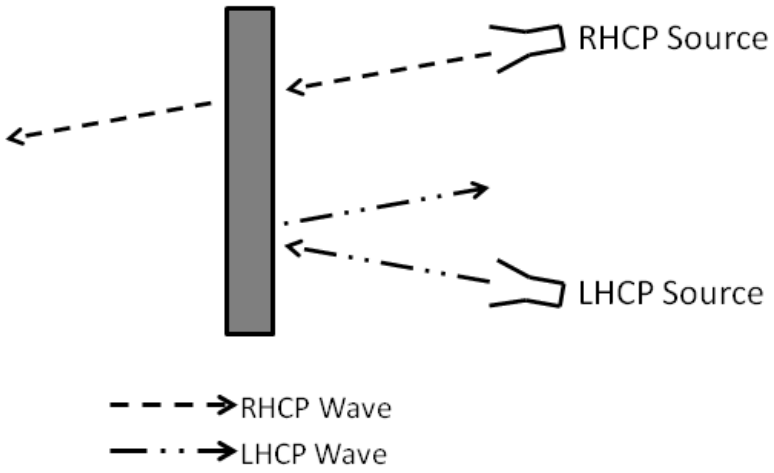

Figure 1.3: Representation of the LHCPSS operation.

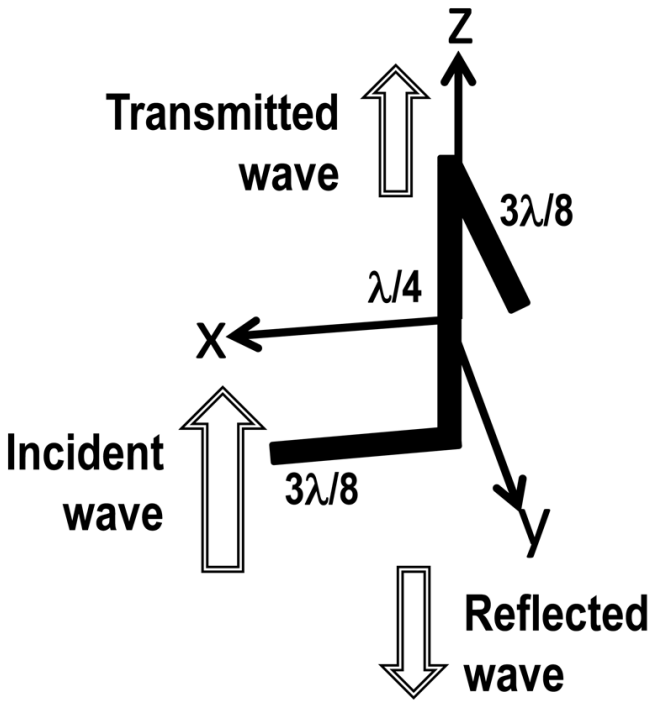

Figure 1.4: Pierrot cell.

1.2 Previous CPSS designs based on the Pierrot cell

There have been many implementations of CPSS made of structures comprising multiple conductive layers, as in the works of Tilston *et al.* (1988), Morin (1990), Roy and Shafai (1996), Tarn and Chung (2007), Joyal and Laurin (2011), Sanz-Fernandez *et al.* (2012) and Mener *et al.* (2012). Morin (1990) fabricated a CPSS based on Pierrot cells made of folded wires bent to achieve the shape shown in Fig. 1.4. Fusco and Nair (2006) also made also a design based on bent wires, with the classical Pierrot cell shape of Fig. 1.4. Each wire was bonded on a low density substrate. Another design in which the vertical segment of the Pierrot cell is implemented with a short wire passing through a low-density honeycomb substrate, and then soldered to the two horizontal segments printed on thin substrates was proposed by Sanz-Fernandez *et al.* (2012). Tarn and Chung (2007) made a design of a CPSS using printed circuit layers. They replaced the vertical segment with electromagnetically coupled lines on different substrate layers. To provide support to the Pierrot cell, a dielectric substrate has to be used. In order to eliminate the need for a substrate, a self-supporting wire in which each cell is mechanically supported by two neighboring cells was proposed by Morin (1995). However, fabricating such a structure could be complicated.

Another important aspect is the dependency of the CPSS performance on the incidence angle. A periodic array design with two cranks per period was proposed by Roy and Shafai (1996). This approach helped reducing the dependency on the angle of incidence. Finally, a bandwidth that is sufficient to support broadband applications is desired. It has been demonstrated by Munk (2005) that in the case of frequency selective surfaces, increasing the density of the cells leads to a better bandwidth and to less sensitivity to variations of the angle of incidence. This is another reason to justify the investigation of increased density double-crank Pierrot cells for the realization of a CPSS.

1.3 Research Objectives

The first objective of this M.A.Sc. work is to study an alternative method of manufacturing a CPSS based on the Pierrot cell using the standard printed circuit technology. The motivation is to eliminate the difficulty of implementing the $\lambda/4$ via, while keeping the $\lambda/4$ segment in the Pierrot cell, and also to allow more flexibility in the Pierrot cell design by taking advantage of the printed circuit technology benefits.

Based on this new fabrication method providing more degrees of freedom for the Pierrot cell design, the second objective is to explore modifications that could make the CPSS more efficient in terms of bandwidth and less dependent on the direction of propagation of the incident wave.

CHAPTER 2

A NEW METHOD FOR THE DESIGN AND FABRICATION OF A CPSS BASED ON PIERROT CELLS

2.1 Introduction

In this chapter we will describe a CPSS made of simple Pierrot unit cells CPSS. We will first study the structure without dielectric substrate and continue with a more realistic CPSS that will actually be fabricated. Also, we will develop the equations needed for the analysis of the structure.

2.2 CPSS in free space

Morin (1990) and Fusco and Nair (2006) have fabricated their CPSS with wires having a circular cross section. Mener *et al.* (2012) used a stacked substrate comprising two thin layers of dielectric substrates separated by a dielectric spacer. Sanz-Fernandez *et al.* (2012) used horizontal printed metallic strips soldered to the vertical wire segments. Instead of using wires with a circular cross section, we propose a design made from thin metal strips printed on a flexible substrate. Three metal strips implement the horizontal and vertical segments of the Pierrot cell, as shown in Figure 2.1. The first horizontal segment is oriented in the direction (ϕ=45 deg, θ=90 deg), the second horizontal segment in the direction (ϕ=135 deg, θ=90 deg) and the vertical segment is in the direction θ=0 deg, with its flat strip parallel to the plane ϕ=90 deg.

As a first step in the design of a CPSS, we begin with the study of a periodic array of Pierrot cells in free space, that is, by assuming there is no solid dielectric substrate. This is consistent with the Pierrot cell description given in the previous chapter. The operating frequency is 20 GHz, which is in the downlink frequency band of future broadband satellite communication systems. The structure in Fig. 2.1 is repeated periodically along two orthogonal directions in the XY plane. The infinite array model is analyzed in Ansys HFSS 15.0 (High Frequency Structure Simulator) which is a software based on finite elements.

To simplify the design, the principal plane (which is the plane formed by the vertical and lower horizontal segment) of the CPSS is at ϕ =45 degrees. This rotation will be necessary when the substrate will be later added to the structure in order to have a symmetric model. An analysis of the symmetry will be done in section 3.3.2. The structure has 2 ports. Port #1 is in the bottom of the structure, while port #2 is on the top. To study the CPSS, we

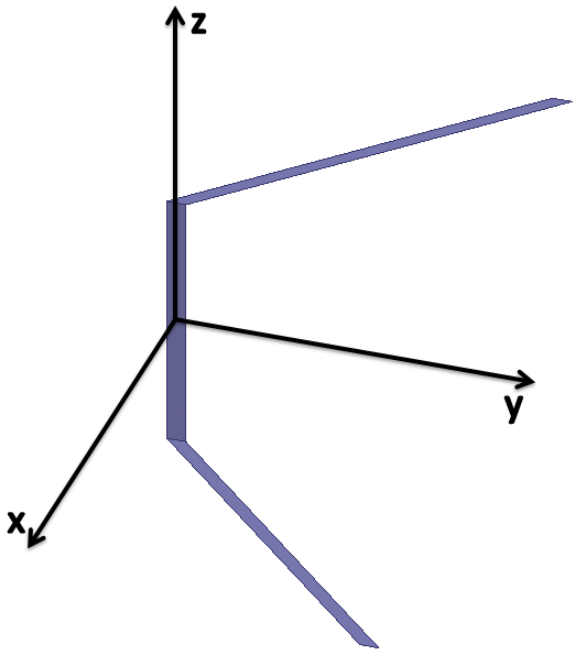

Figure 2.1: Model of a single element of a CPSS based in the Pierrot cell.

use the HFSS analysis based on Floquet ports to analyze an infinite periodic structure. With this approach, it is sufficient to simulate only one cell. We choose two modes at each port for the Floquet analysis (see Bhattacharyya, 2006). The E vector for modes 1 and 2 are in the "$\hat{x}$" and "$\hat{y}$" directions respectively. This leads to an S matrix with dimensions of 4×4. This matrix has the following form :

$$\mathbf{S} = \begin{bmatrix} S(1:1,1:1) & S(1:1,1:2) & S(1:1,2:1) & S(1:1,2:2) \\ S(1:2,1:1) & S(1:1,2:2) & S(1:2,2:1) & S(1:2,2:2) \\ S(2:1,1:1) & S(2:1,1:2) & S(2:1,2:1) & S(2:1,2:2) \\ S(2:2,1:1) & S(2:2,1:2) & S(2:2,2:1) & S(2:2,2:2) \end{bmatrix}$$

where each matrix element is indicated as S(output port :output mode, input port :input mode), where *port* is the number of the port of the network and *mode* is the number of the Floquet mode.

For example, if we are interested in the transmission to port 2 when we excite port 1, we use :

$$\mathbf{S_{21}} = \begin{bmatrix} S(2:1,1:1) & S(2:1,1:2) \\ S(2:2,1:1) & S(2:2,1:2) \end{bmatrix}$$

where the index j of S_{ij} designates the input port and i the output port.

The S parameters calculated by HFSS are for linearly polarized (LP) modes but for the

CPSS application we are interested to have these parameters for right and left hand circularly polarized (CP) modes. The CP S parameters can be obtained from the LP S parameters as follows. Taking again the example of transmission from port 1 to port 2, we have the relation :

$$\begin{bmatrix} b_1 \\ b_2 \end{bmatrix} = [\mathbf{S_{21}}] \begin{bmatrix} a_1 \\ a_2 \end{bmatrix} \tag{2.1}$$

where a_i are the LP incident wave coefficients, b_j are the LP transmitted wave coefficients whereas indices *1* and *2* refer to the Floquet modes.

A RHCP wave propagating in the $+z$ direction of unitary amplitude has the following form (see Jordan and Balmain, 1968).

$$a_r = \frac{1}{\sqrt{2}} \begin{bmatrix} 1 \\ -j \end{bmatrix} \tag{2.2}$$

While a LHCP wave propagating in the same direction has the form :

$$a_l = \frac{1}{\sqrt{2}} \begin{bmatrix} 1 \\ +j \end{bmatrix} \tag{2.3}$$

From here on, subscripts r and l will be used to designate right and left hand circular polarizations respectively. To obtain the transmitted wave b when the incident wave is RHCP, we insert 2.2 into 2.1 and we obtain :

$$\mathbf{B_{LP}^{tR}} \equiv \begin{bmatrix} b_1^{tR} \\ b_2^{tR} \end{bmatrix} = \frac{1}{\sqrt{2}} \begin{bmatrix} S(2:1,1:1) & S(2:1,1:2) \\ S(2:2,1:1) & S(2:2,1:2) \end{bmatrix} \begin{bmatrix} 1 \\ -j \end{bmatrix} =$$

$$\frac{1}{\sqrt{2}} \begin{bmatrix} S(2:1,1:1) - jS(2:1,1:2) \\ S(2:2,1:1) - jS(2:2,1:2) \end{bmatrix} \tag{2.4}$$

where B_{LP}^{tR} is the vector formed by the transmitted wave coefficients in the LP modes at port 2, for an incident RHCP wave at port 1.

In a similar way, we can develop the equations of the transmitted waves into LP modes 1 and 2 for the case of LHCP incidence and the reflected waves in the two LP modes, for both RHCP and LHCP. The equations are shown in the Appendix A.

To calculate the coefficients of the waves transmitted and reflected in the desired CP modes, the LP transmitted modes have to be projected onto the CP modes (see Jordan and Balmain, 1968). These modes are given by 2.2 and 2.3 in the case of transmitted waves propagating along the $+z$ direction. This projection leads to :

$$\mathbf{B_{CP}^{tR}} \equiv \begin{bmatrix} b_r^{tR} \\ b_l^{tR} \end{bmatrix} = \begin{bmatrix} a_r & a_l \end{bmatrix}^T \mathbf{B_{LP}^{tR}} \tag{2.5}$$

where "T" indicates a transposed complex conjugate matrix.

For example, if we want to know the transmitted RHCP and LHCP wave coefficients when the incident wave is a RHCP, the preceding equation leads to :

$$b_r^{tR} = \frac{1}{\sqrt{2}}(b_1^{tR} + jb_2^{tR}) \tag{2.6}$$

$$b_l^{tR} = \frac{1}{\sqrt{2}}(b_1^{tR} - jb_2^{tR}) \tag{2.7}$$

Once again, the superscript t indicates a transmitted wave and the superscript R specifies an incident RHCP wave. The full set of equations including the case of LHCP incidence and the reflected CP components is given in Appendix A.

For making a full analysis of our CPSS, we also need to calculate the axial ratio (AR). The AR is given by :

$$AR = \frac{\left|b_r^{uV}\right| + \left|b_l^{uV}\right|}{||b_r^{uV}| - |b_l^{uV}||} \tag{2.8}$$

where u=t or r, and V=R or L.

Four definitions of bandwidth will be used in this work. The BW-R is the frequency bandwidth for which the reflection coefficient b_l^{rL} is higher than -3 dB and the BW-T is the bandwidth for which the transmission coefficient b_l^{tL} is smaller than -3 dB. Both definitions are used in the case of LHCP incidence. This is a consequence of an arbitrary choice of working with LHCPSS only in this research. Of course, the results found with the LHCPSS are directly applicable to the RHCPSS, which is obtained by a simple change of geometry. Also, the fact that both BW definitions apply to LHCP incidence is due to the fact that the desired LHCP response is much more narrow-band than the RHCP response. Therefore, it

is really the LHCP response that will define the usable bandwidth of a LHCPSS. The other two types of bandwidth are the B-AR$_t$ and B-AR$_r$ which are the frequency range for which the axial ratios of the transmitted RHCP and reflected LHCP waves are respectively below 1 dB.

2.2.1 Simulation of the CPSS in free space

Now that we have all the equations for a complete analysis of the CPSS, we start with the simulations in HFSS. The first model is a CPSS in free space. The initial lengths of the cell segments are those given in Fig. 1.4. The unit cell dimensions were 10 mm $\times$ 10 mm along the x and y axes, which correspond to $0.66\lambda \times 0.66\lambda$ at the design frequency of 20 GHz. These dimensions were chosen in order to allow the segments to have considerable larger dimensions than those in Fig. 1.4. This would allow HFSS Optimetrics to adjust the dimensions without disturbing the model, especially when we have a complete model that actually could be built (see section 2.3). The lengths of the horizontal and the vertical segments, and the width of all the segments were optimized to maximize transmission of the RHCP waves and reflection of the LHCP waves. Two optimization goals with equal weight were used, namely $\left|b_r^{tR}\right| = 1$ and $\left|b_l^{rL}\right| = 1$ at a frequency of 20 GHz. These objectives correspond to a LHCPSS, i.e. a CPSS having total transmission for an incident RHCP wave and total reflection for an incident LHCP wave. The optimization in HFSS was done with the Quasi Newton method. This method is adequate for local optimization, which means that an initial guess close enough to the optimal solution has to be given in order to avoid trapping in local minima. This iterations were continued until the variation in dimensions became considerably small, that is less than 1 mil. Then, the obtained dimensions were used in the final model.

Fig. 2.2 shows the results for the case of RHCP incidence (equations A.9 and A.11 for the RHCP transmission coefficients and reflection coefficients respectively). Fig. 2.3 shows the results for the LHCP incidence (equations A.14 and A.16 for the LHCP transmission coefficients and reflection coefficients respectively). From these figures, we observe that the CPSS has both LHCP reflection coefficient and RHCP transmission coefficient of 0 dB at 20 GHz. In these simulations perfect electric conductors were assumed for the Pierrot cell elements. We can also observe that the minimum RHCP reflection coefficient is not exactly at the desired frequency, however at 20 GHz the RHCP reflection is almost at -30 dB, which is quite low. In terms of the bandwidth, we can see that the BW-T is 11% (2.21 GHz). Fig. 2.4 shows the results for the reflection (for LHCP incidence) and transmission (for RHCP incidence) AR (equation 2.8). Here we see that both the transmission and reflection AR have the same value of 0.01 dB at 20 GHz. The axial ratio of the reflected wave in case of LHCP incidence is below 1 dB in the 18-21 GHz frequency band, which is a band of interest

for satellite communications. The axial ratio of the transmitted wave for RHCP incidence is below 1 dB over the whole frequency interval considered. Though this CPSS cannot be fabricated because it needs some kind of mechanical support, in the next section we will discuss the chosen method of giving support to the CPSS.

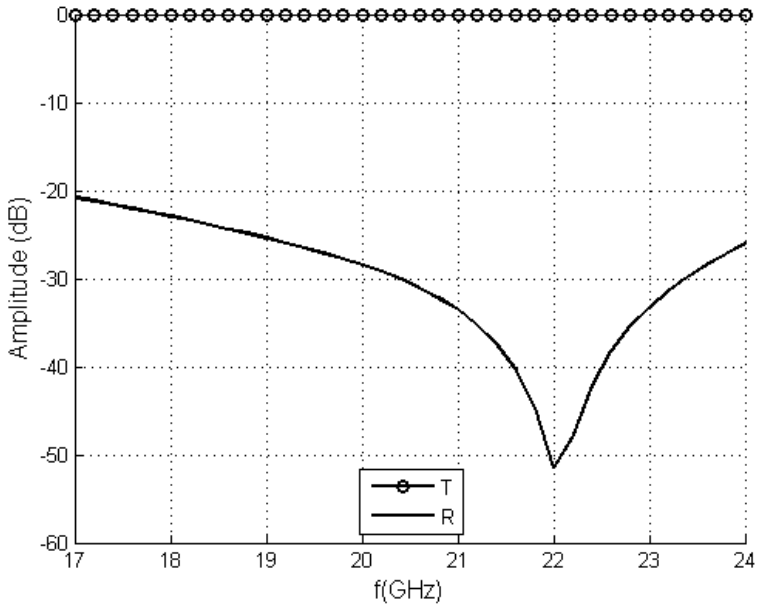

Figure 2.2: RHCP transmission and reflection coefficients for the CPSS in free space for the case of RHCP incidence. $T = |b_r^{tR}|$ and $R = |b_r^{rR}|$.

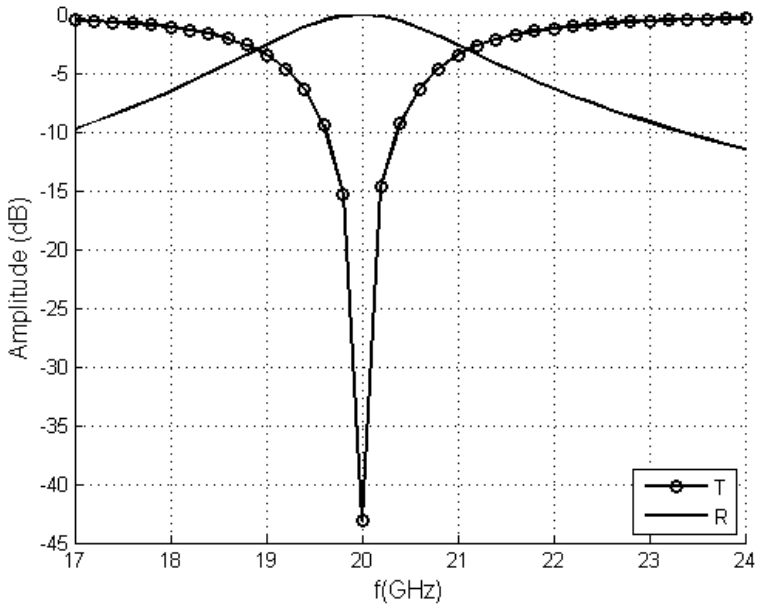

Figure 2.3: LHCP transmission and reflection coefficients for the CPSS in free space for the case of LHCP incidence. $T = |b_l^{tL}|$ and $R = |b_l^{rL}|$.

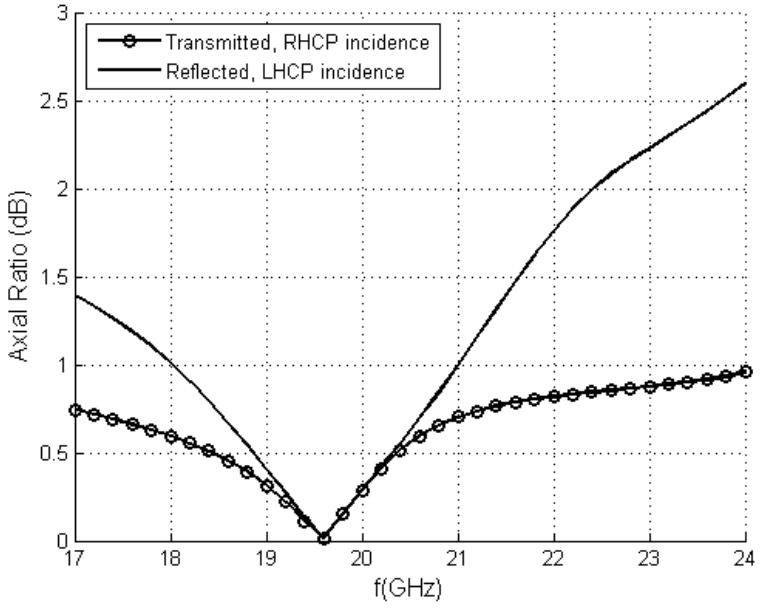

Figure 2.4: Transmission (for RHCP incidence) and reflection (for LHCP incidence) AR for the CPSS in free space.

2.3 Support and Optimization of the CPSS

To be able to fabricate the Pierrot cells, we need some kind of support. The original solution proposed in this work is to implement the CPSS on a folded flexible substrate. The cell itself is made of thin printed strips on such substrate. Each strip implements the vertical and horizontal segments of the CPSS. To arrive to the desired shape of the Pierrot cell, the substrate is folded along lines going through the junctions of the horizontal and vertical segments. The folded substrate is placed over a piece of foam machined to form a crenellated grating. Another piece of foam is placed over the substrate. Figs. 2.5, 2.6 and 2.7 shows a 3D view, top view and lateral view of the model respectively. The cells form an array along the x and y directions. The horizontal arms are rotated by 45 degrees with respect of the x and y axes and have the same orientation with respect to the vertical walls. This improves the symmetry of the design. These arms are at levels $z = \lambda/8$ and $z = -\lambda/8$.

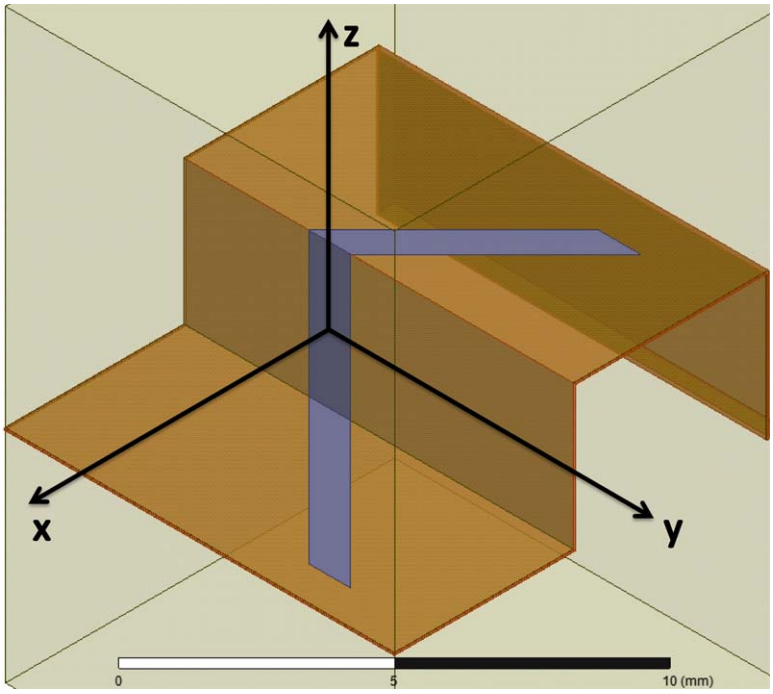

Figure 2.5: 3D view of a single unit Pierrot cell used for simulations.

The substrate chosen for the structure is Pyralux AP 8525R from Dupont, with thickness of 0.0508 mm (2 mils). Table 2.1 shows its electrical characteristics at 20 GHz. These values were measured by our team. This substrate was chosen because it is easily foldable and has low losses.

We have considered three types of foam from Evonik (see Table 2.2, values specified by the manufacturer at 26.5 GHz) to support the structure. The cell was optimized according to the

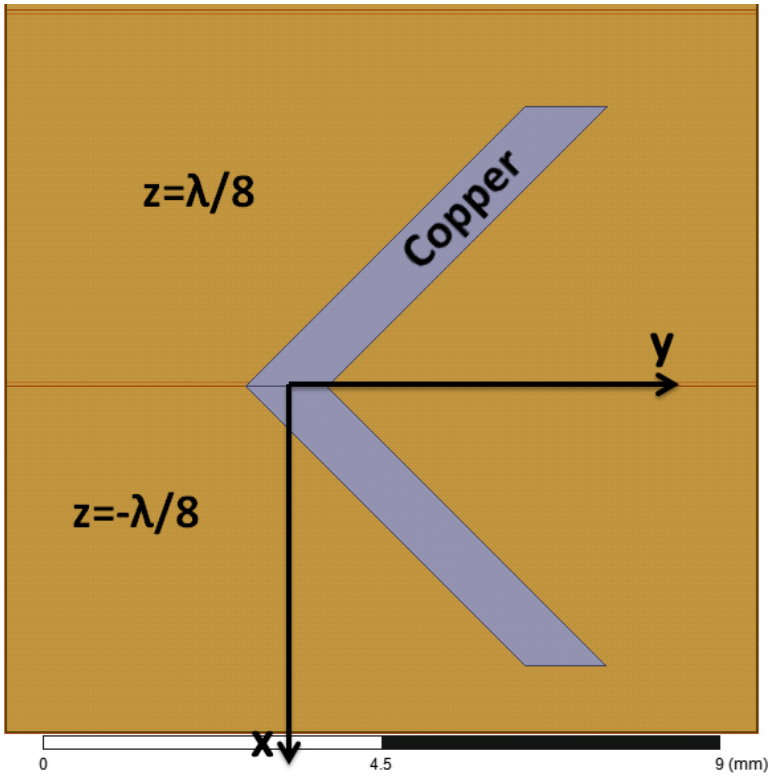

Figure 2.6: Top view of the model of a single unit Pierrot cell used for simulations.

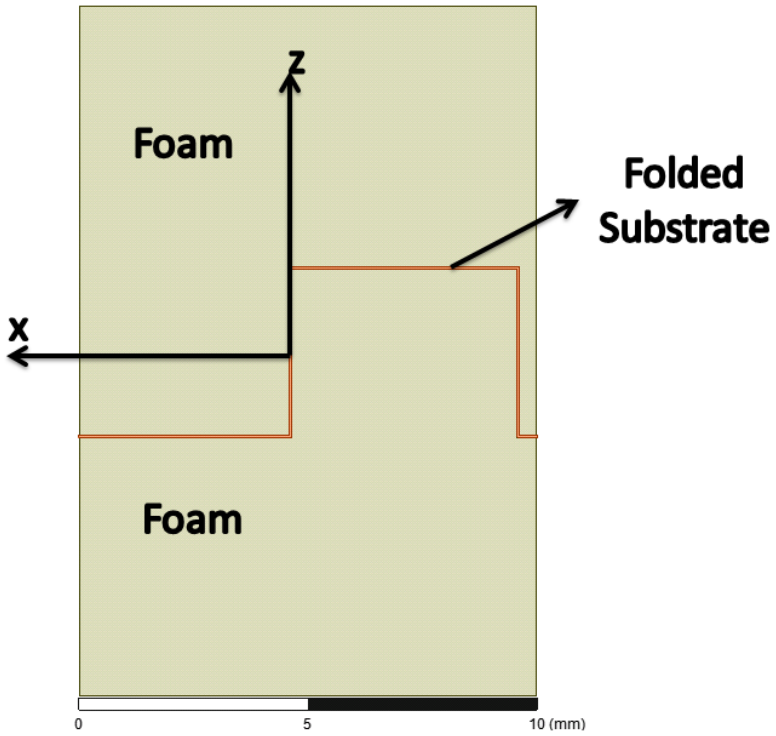

Figure 2.7: Side view of the model of a single unit Pierrot cell used for simulations.

Table 2.1: Characteristics of the substrate Pyralux AP 8525R at 20 GHz.

	ϵ_r	tanδ
Pyralux AP 8525R	3.4	0.002

criteria mentioned previously for the CPSS, assuming Rohacell 71HF as a support material. Figs. 2.8 and 2.9 show a comparison of the results of the RHCP transmission coefficients and the LHCP reflection coefficients respectively for a LHCPSS implemented with the three different types of foam. In theses simulations, the total thickness of the two foam layers, as shown in Fig. 2.7, was set to 15 mm, which is the value of λ in free space. The RHCP transmission coefficients for the CPSS using Rohacell 31HF is -0.34 dB at 20 GHz while the other types of foam lead to more insertion loss. With respect to the LHCP reflection coefficients, Rohacell 31 HF led to a peak value of -0.85 dB while the other foams gave higher return loss. So, Rohacell 31HF provides the best results in terms of losses, and it was therefore chosen for fabricate the CPSS prototypes.

Table 2.2: Characteristics of the Rohacell foams from Evonik at 26.5 GHz.

foam	ϵ_r	tanδ
Rohacell 31HF	1.041	0.0106
Rohacell 51HF	1.048	0.0135
Rohacell 71HF	1.093	0.0155

As observed by Munk (2005) with frequency selective surfaces, choosing an adequate spatial density of cells can lead to less dependency of the transmission and reflection characteristics on the angle of incidence and it can also lead to a better frequency bandwidth. It can be conjectured that similar trends could also be observed in other periodic structures, such as the CPSS. In order to choose a good density, we simulated the model in Fig. 2.5 with three different cell periods (8.5 mm $\times$ 8.5 mm, 9 mm $\times$ 9 mm and 10 mm $\times$ 10 mm). The results for the RHCP transmission coefficient and the LHCP reflection coefficient are shown in Figs. 2.10 and 2.11 respectively. As it can be seen, none of the three cell sizes has a clear advantage over the others. The 8.5 mm cells give the best bandwidth in terms of b_l^{rL} whereas the 9.5 mm cells give the best b_r^{tR} bandwidth but the worst b_l^{rL} bandwidth. The 10 mm cells seem to be a good compromise. We therefore choose the period of 10 mm $\times$ 10 mm in our designs. The physical characteristics of the cell are shown in Table 2.3. The lengths of the optimal segments differ slightly from the nominal values shown in Fig. 1.4. The optimal length of the horizontal segments is 5.56 mm instead of 5.625 mm and for the vertical segment the length is 3.78 mm instead of 3.75 mm. Of course, this optimization is carried-out with the Pierrot cell in presence of the Pyralux and foam substrates, whereas the nominal segment lengths

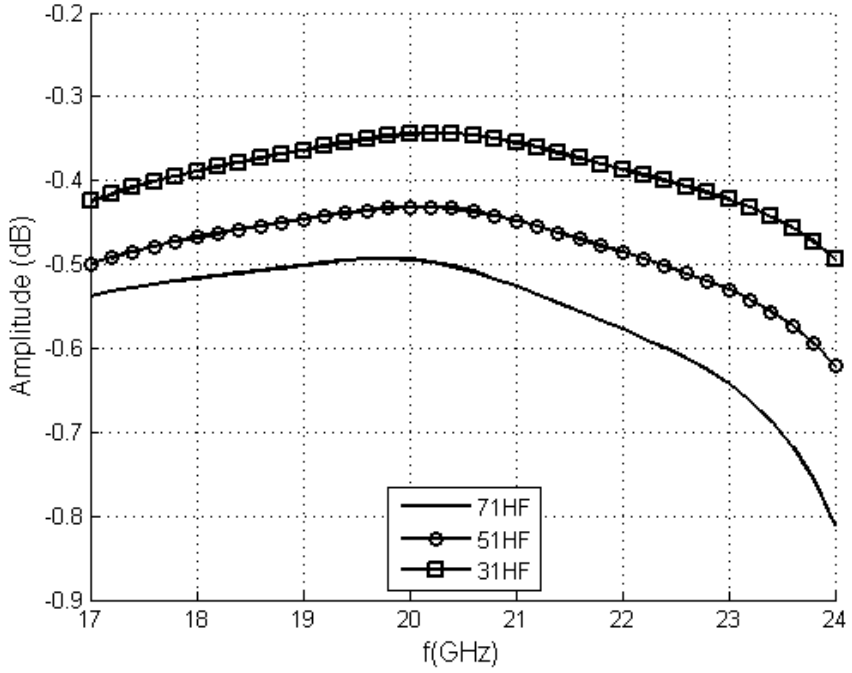

Figure 2.8: RHCP transmission coefficient (b_r^{tR}) for three types of foam.

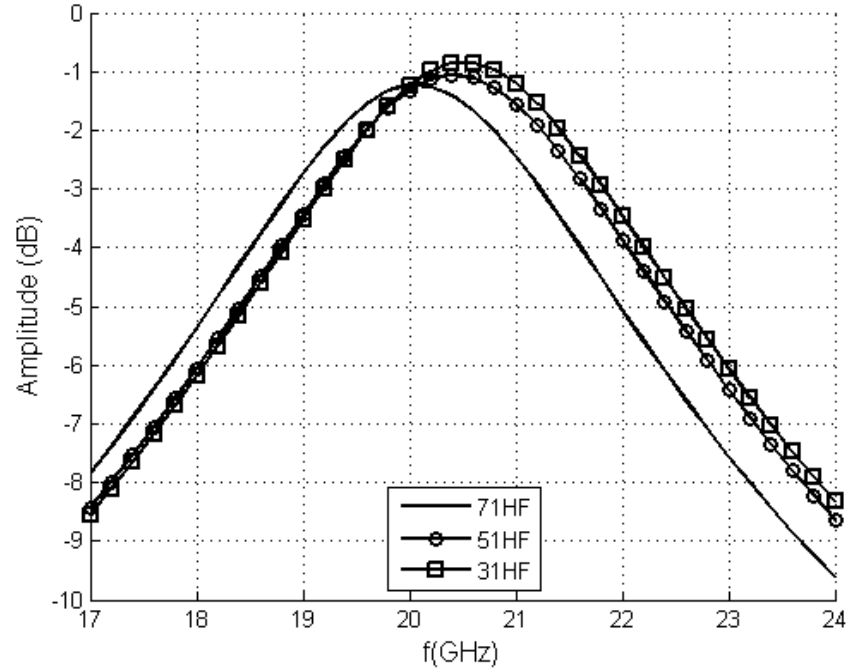

Figure 2.9: LHCP reflection coefficient (b_l^{rL}) for three types of foam.

assumed Pierrot cells surrounded by air.

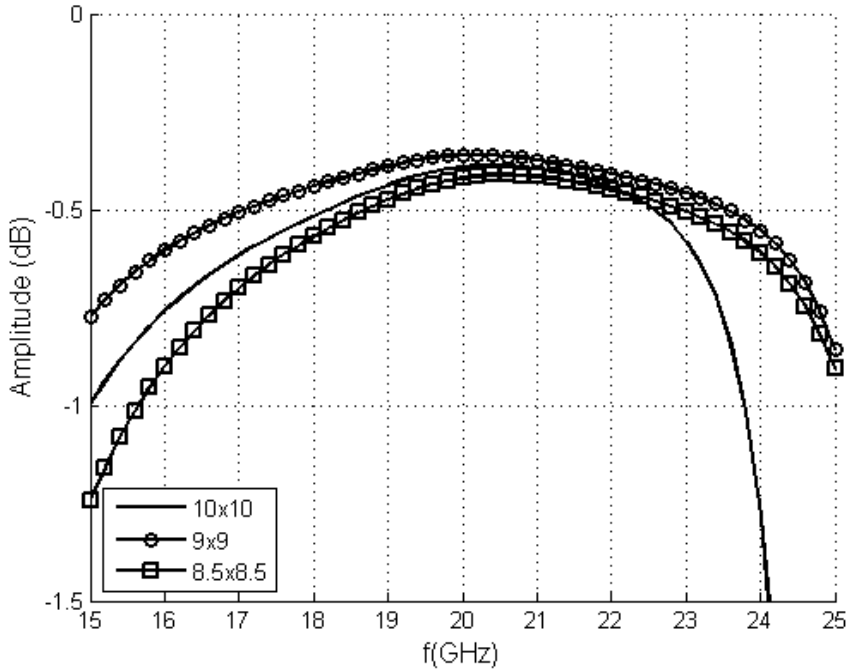

Figure 2.10: Transmission coefficient of the RHCP wave (b_r^{tR}) as a function of frequency for different cell periods.

Table 2.3: Physical characteristics of the optimized Pierrot unit cell implemented on a 2 mils Pyralux substrate with Rohacell 31HF support layers.

Period	10 mm × 10 mm
Horizontal segments length	5.56 mm
Vertical segment length	3.78 mm
Segments width	1.32 mm

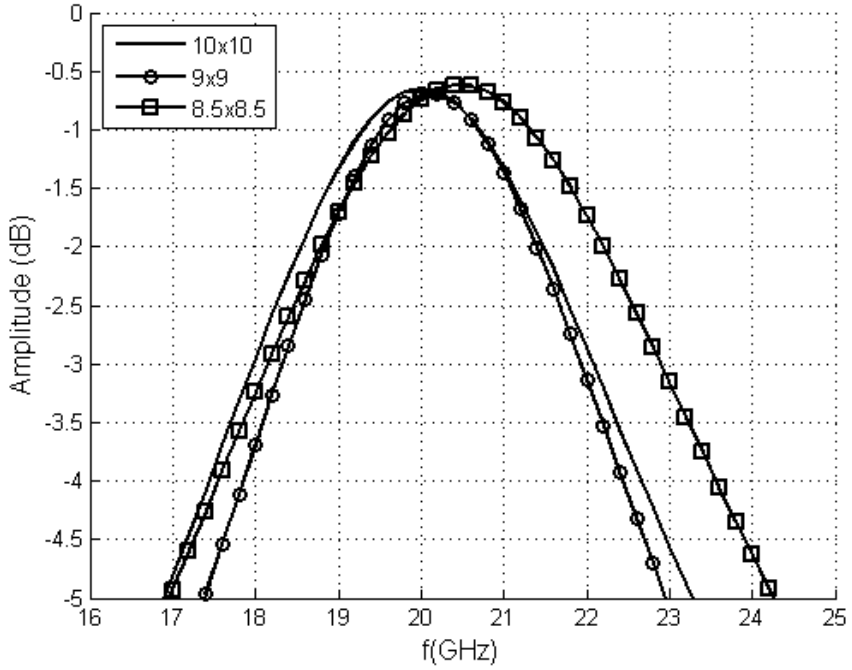

Figure 2.11: Reflection coefficient of the LHCP wave (b_l^{rL}) as a function of frequency for different cell periods.

2.4 Fabrication and measurement of the CPSS prototype

With the optimized lengths of the cell (Table 2.3), we proceeded to the fabrication of a prototype using a standard printed circuit board process. Fig. 2.12 shows a printed pattern obtained after chemical etching. Four patterns were needed to arrive to the desired dimensions of the whole CPSS because of a size limitation in our etching equipment. The holes on the sides of the substrate are used to hold the pyralux sheet in a special tool that has been manufactured to fold the circuit. Fig. 2.13 shows this tool with pins to hold the etched substrate on both sides. To obtain the desired crenellated profile, this tool was designed to allow the substrate to have the sharpest possible 90-degree folds. After folding, the four patterns were cut in order to remove the holes and cover a surface of 20 cm $\times$ 20 cm.

Two pieces of foam (as described in section 2.3) were machined to support the structure. Then, the folded substrates were placed on a foam piece, as illustrated in Fig. 2.14. Another piece of foam was added to complete the CPSS and keep the printed circuit board folded, as shown in Fig. 2.15. With this method, no adhesive layer is used. This avoids losses in the adhesive and keeps the assembly process very simple. The dimensions of the finished CPSS are 20 cm $\times$ 20 cm $\times$ 2.192 cm and the number of cells is 20 by 19. Each groove in the foam has a width of 5 mm and a depth of 3.78 mm, which corresponds to the optimized length of

the vertical segment.

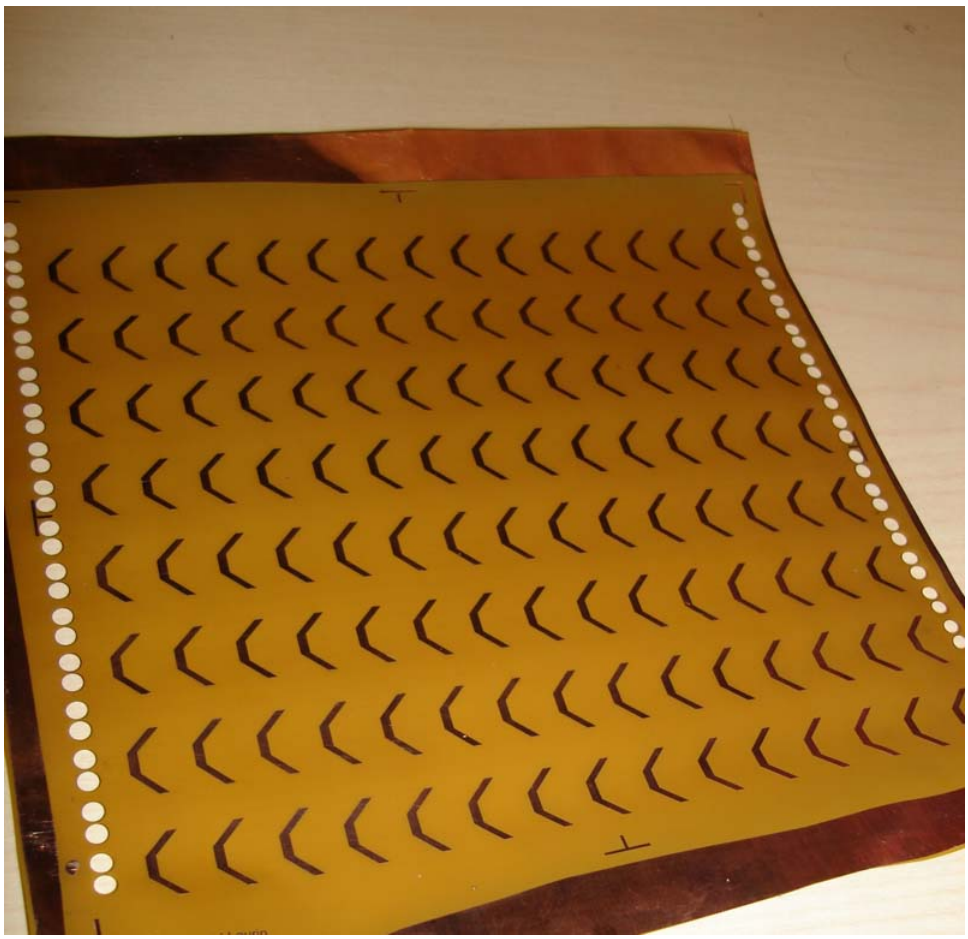

Figure 2.12: Printed pattern of the CPSS before the folding process.

We characterized the CPSS with a test bench operating in free space. This bench is composed of two horn antennas, one on each side of the prototype. Additionally, two lenses are used to illuminate the CPSS with a planar phase front. The horn antennas are connected to an HP8501C network analyzer. To minimize the effects of multiple reflections between the CPSS, the lenses and the antennas, we used a "line-reflect-match" (LRM) calibration and also "time gating". This way we can reduce the ripples on the measured responses. In guided waves S-parameter measurements (e.g. in coaxial and printed lines and in rectangular waveguides), calibration is usually sufficient to remove undesired reflections and time gating is not necessary. In free-space measurements, more than one mode can be present at the same time (e.g. horizontal and vertical polarizations). The calibration can be done for both modes separately with appropriate calibration standards. However, since the tested CPSS is non ideal, there is some coupling between the two orthogonal polarizations. Removing multiple reflections due to cross-polarized components would require a 4-port calibration procedure,

Figure 2.13: Tool fabricated for the folding process.

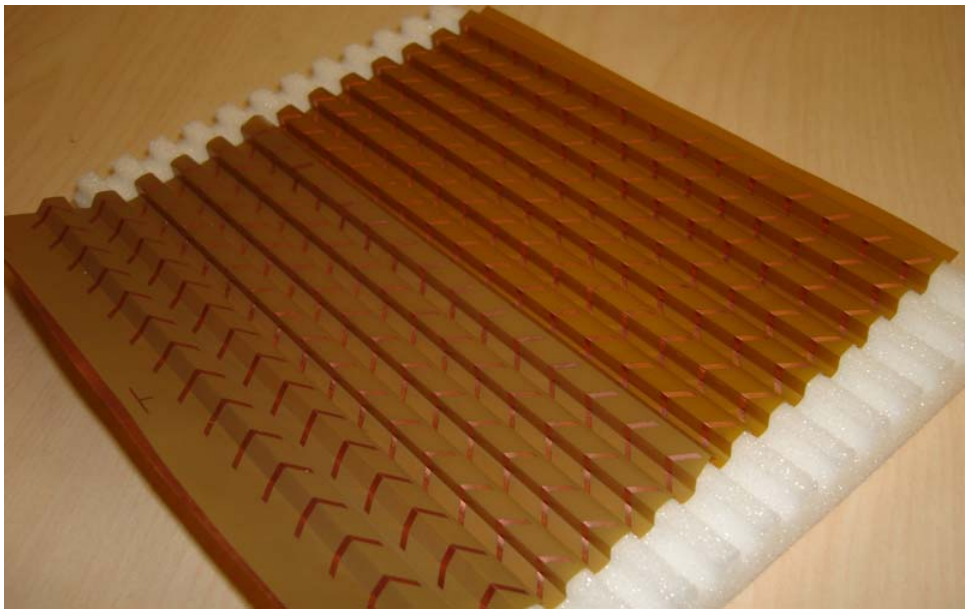

Figure 2.14: Folded structure over a piece of machined foam support. The edges of the substrate has been cut away to remove the holes.

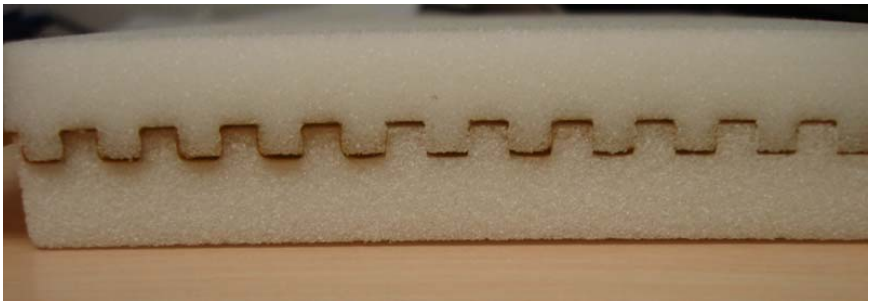

Figure 2.15: Lateral view of the assembled CPSS.

which is not available with the test setup at hand (for instance orthomode transducers would be required to separate the two modes at each port). Consequently, time gating was used to remove reflections that could not be handled by the 2-port LRM calibration. Fig. 2.16 shows the test bench. The horn antennas work in the linear polarization. In order to analyse the circular polarization, we take measurements in two orthogonal polarizations by pivoting the horns around the main beam axis and combine the results to reproduce circular polarization. This procedure was also done in simulation with the Floquet modes described in section 2.2. The same equations in Appendix A and in the previous section are used to calculate the reflection and transmission parameters of the CP waves. Only the transmission results will be presented in this work. In order to have the results for the reflection, we would need antennas capable of transmitting and receiving at the same time in two orthogonal polarizations. This is possible by adding orthomode tranducers on the horn antennas. Unfortunately such transducers were not available in our laboratory.

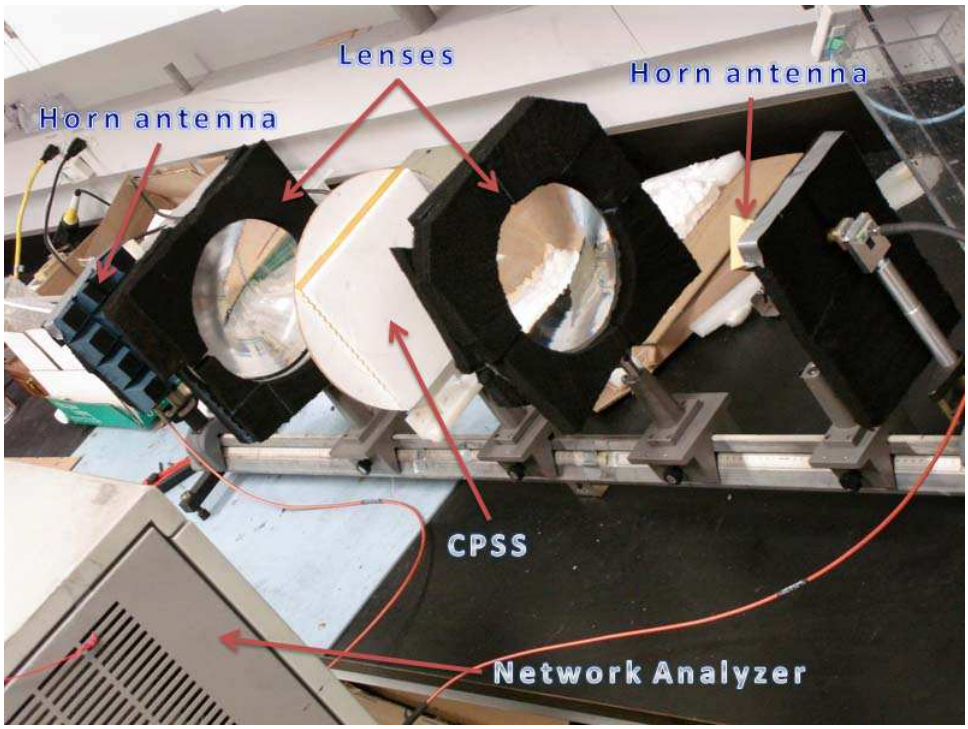

Figure 2.16: Test bench used to characterize the CPSS.

Fig. 2.17 shows a comparison between measurements and simulations for the RHCP and LHCP transmission coefficients. At 20 GHz, the measured LHCP and RHCP transmission coefficients are -20.7 dB and -0.5 dB, respectively. In comparison, the simulations gives the corresponding values of -24 dB and -0.5 dB. We observe a small gain for the RHCP transmission coefficients on a portion of the bandwidth measured in Fig. 2.17. Hopkins *et al.*

(2010) have studied this effect and it was attributed to a focusing effect by the periodic structure that occurs with non-uniform amplitude illuminations. Since uniform illumination is not possible in practice, it is not possible to remove this effect. In terms of the bandwidth, the simulated and measured BW-T are 27% (5.44 GHz) and 17.6% (3.53 GHz). Fig. 2.18 shows the transmission AR. We observe that at 20 GHz, the measured AR is 1.32 dB versus 0.24 dB for the simulation. However, the minimum of 0.22 dB has shifted to 20.8 GHz. Additionally, the best B-AR_t performance has shifted to the frequency band of 20.19-21.59 GHz in comparison to the frequency band of 18.49-21.26 GHz for the simulated results. The differences between simulations and measurements can be attributed to systematic measurement errors caused by the non uniform illumination of the samples, fabrication errors in the etching and folding of the substrates and inaccuracies in the material properties used for the simulations.

The foam layers are the main cause for the losses in the CPSS. Even with those layers, this CPSS offers better performances than those presented in the works of Morin (1990) and Fusco and Nair (2006) which uses also the Pierrot cell. In these works, the highest RHCP transmission coefficients were -2 dB and -4 dB respectively, which is significantly less than the results in Fig. 2.17. These references obtained LHCP transmission coefficients of -25 dB and -18 dB (at frequencies of 7.5 GHz and 9.8 GHz respectively) which compares well with our results. In the following chapters, we will compare other variants of the proposed CPSS with the objective of improving performance.

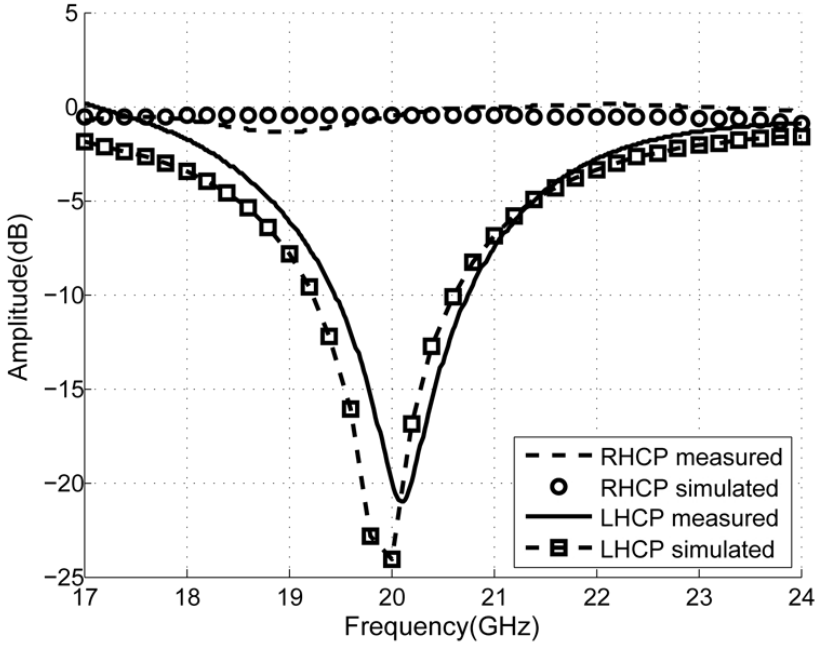

Figure 2.17: Measurements vs. simulations of the RHCP and LHCP transmission coefficients for the fabricated CPSS prototype.

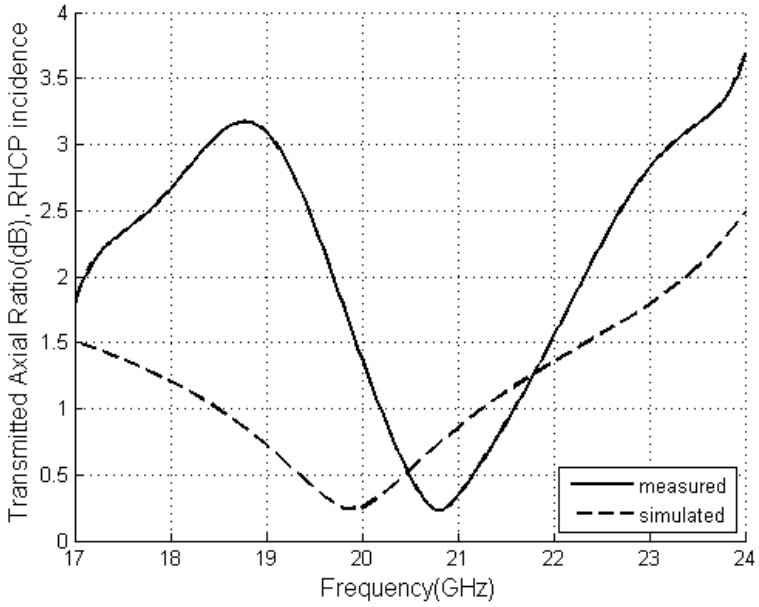

Figure 2.18: Measurements vs. simulations for transmission AR for the fabricated CPSS prototype.

CHAPTER 3

PERFORMANCE ENHANCEMENT OF THE PRINTED CPSS

3.1 Introduction

In this chapter we analyze four variants of the Pierrot cell with the objective of improving the performance of the CPSS. We will start with a Pierrot cell with a load in the middle segment. We then continue with a cell at 90 degrees that is printed on only two planes of the folded substrate instead of three for the normal Pierrot cell. Then, we also discuss two variants of the double Pierrot cell. We complete this chapter with an analysis of the foam support for the CPSS.

3.2 Pierrot Cell with Load in the Middle Segment

In a LHCPSS, cross polarization consists of reflected RHCP waves (b_r^{rR}) and transmitted LHCP waves (b_l^{tL}). In a dual-grid reflector system, as in satellite antennas used for communications and remote sensing, the control of cross-polarization is very important. In a CPSS design it would be desirable to minimize these two wave components at the design frequency. Unfortunately, in Pierrot cells the frequency at which the reflected cross-polarization is minimized, is different than the frequency where minimum cross polarization in transmission occurs. Fig. 3.1 shows the cross-polarization under RCHP and LHCP illumination for the simple unit cell studied in section 2.3. The minimum for the LHCP waves is at 20 GHz while the minimum for the RHCP waves is at 22.2 GHz.

This effect is related to shifts of the resonance and antiresonance frequencies of the wire or trace forming the unit cell. Let us consider the unfolded current distribution of a LHCPSS unit cell (see Roy and Shafai, 1996). Under RHCP illumination the antiresonance current distribution has a quasi-uniform phase and it does not have a null in the centre of the wire. Under LHCP illumination the two halves of the cell have currents that are out of phase by 180 degrees and there is a null in the centre. Because of this null, it is possible to insert a lumped load at the center of the wire without disturbing the operation of the CPSS under LHCP operation, while affecting the centre current present in the RHCP illumination. Based on this principle, we propose a cell with a load in the vertical segment in order to reduce the current on the cell under RHCP illumination at the design frequency.

Fig. 3.2 shows the 3D model of this proposed cell. Instead of packaged components that would need soldering on each cell of the CPSS, we are taking advantage of the printed circuit

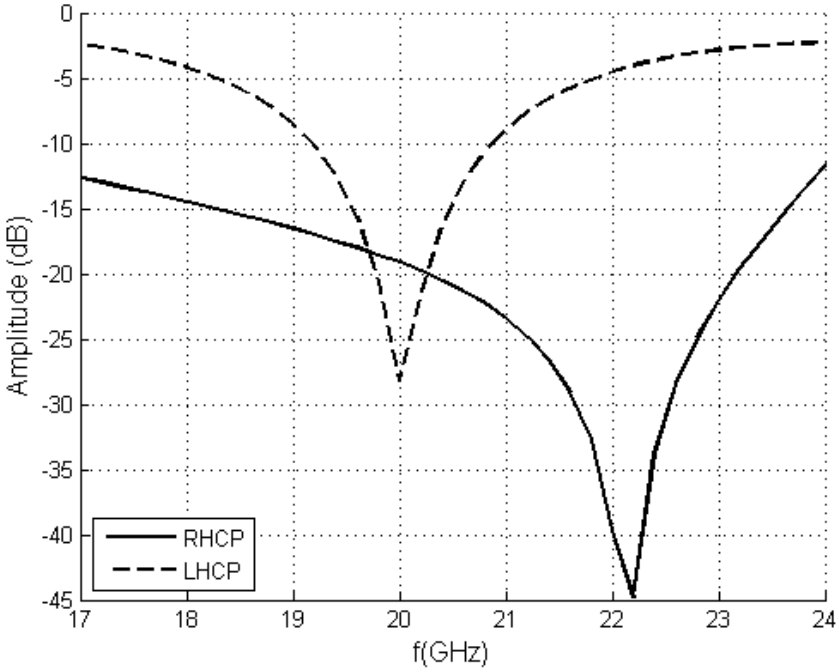

Figure 3.1: Simulation results for the cross-polarization under RCHP (b_r^{rR}) and LHCP (b_l^{tL}) illumination for the simple unit cell in section 2.3.

implementation proposed in the previous chapter to implement the load in a printed form. In Fig. 3.2 we have used a short meander line printed on the same substrate as the Pierrot cells to implement a series inductive load. Although small, this line is exposed to the incident field, so its effect is not exactly that of a lumped load. A LHCPSS including this new cell was designed. The cell period is 10 mm $\times$ 10 mm, as with the LHCPSS simple unloaded unit cell shown in Fig. 2.5. The lengths of the segments were optimized to maximize the LHCP reflection and the RHCP transmission, and minimize LHCP transmission and the RHCP reflection, all of them at the design frequency of 20 GHz. These equations are in Table 3.1. The weight of each condition in the objective function to optimize is the same. The final lengths of the segments are indicated in Table 3.2

Table 3.1: CPSS optimisation criteria used in HFSS for the loaded Pierrot cell.

$\left\|b_r^{tR}\right\| = 1$
$\left\|b_r^{rR}\right\| = 0$
$\left\|b_l^{tL}\right\| = 0$
$\left\|b_l^{rL}\right\| = 1$

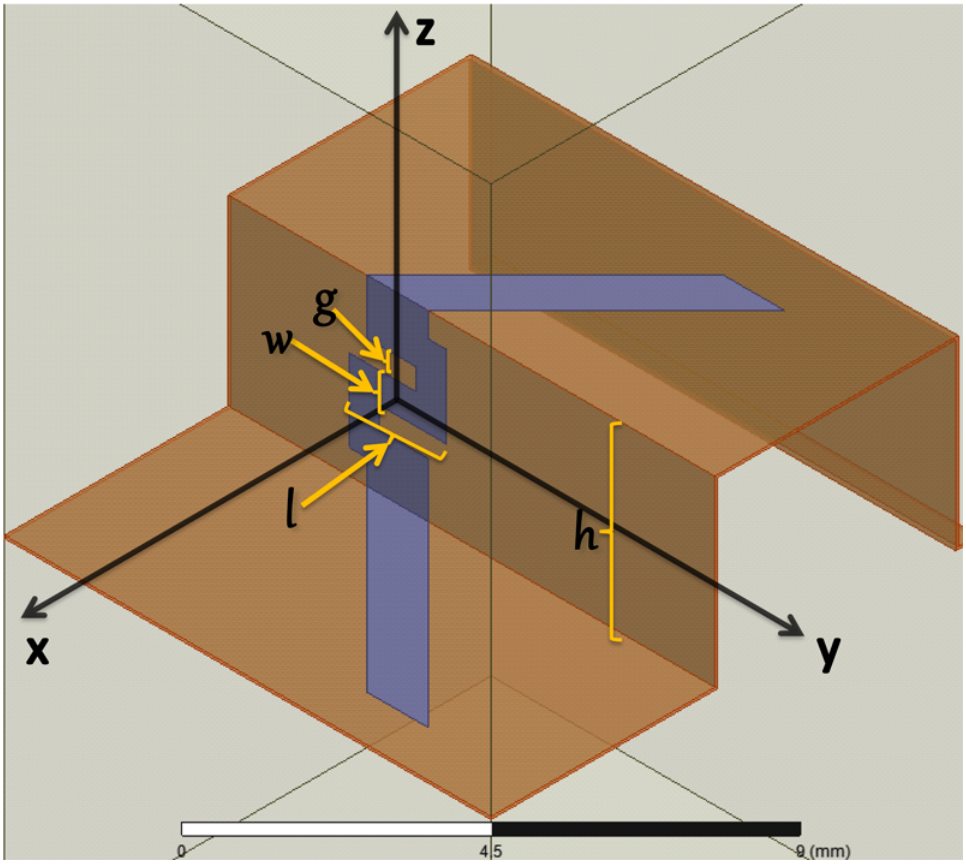

Figure 3.2: 3D model of the Pierrot cell with a load in the middle.

Table 3.2: Physical characteristics of the optimized single unit Pierrot cell CPSS with a load.

Period	10 mm × 10 mm
Horizontal segments length	5.18 mm
Horizontal segments width	1.25 mm
Vertical height h	3.75 mm
Gap g between the strips	0.44 mm
Width w of the strips in the vertical wall	0.62 mm
Length l of the horizontal segment of the load	2 mm

Figs. 3.3 and 3.4 show a comparison of the simulated results for the transmission and reflection coefficients for the loaded and unloaded cell cases. A useful metric on the level of regarding the cross-polarization is the co-pol to cross-pol ratio for the RHCP waves defined as follows :

$$\frac{b_r^{tR}}{b_r^{rR}} \tag{3.1}$$

Similarly, a co-pol to cross-pol ratio metric for the LHCP waves can be defined :

$$\frac{b_l^{rL}}{b_l^{tL}} \tag{3.2}$$

It should be noted that these metrics differ from the usual co-pol to cross-pol ratio used for instance in antenna pattern measurements. In this case both polarizations are measured at the same physical port, whereas in (3.1) and (3.2) the two quantities are measured at different ports (one is transmitted and the other is reflected). However, given the desired operation of the CPSS as a discriminator of polarization between transmitted and reflected waves, these metrics are meaningful in assessing the quality of the realized CPSS. Figs. 3.5 and 3.6 shows these ratios for the RHCP and LHCP waves respectively. We can be observe that although the optimization was done for a single frequency of 20 GHz, the best performance is obtained at about 19.7 GHz. To achieve the best performance at the desired frequency, we could do a slight geometrical downscaling of all the dimensions. Nevertheless, it is clear that loading the structure has led to significant improvements. First of all, the frequency for minimum reflection under RHCP illumination has shifted down from 22.2 GHz to 19.7 GHz, with a reduction from -19 to -28 dB at 20 GHz. This frequency now coincides with the frequency for minimum transmission under LHCP illumination, as desired. Both loaded and unloaded cells have similar transmission coefficients for the RHCP waves. Regarding the LHCP waves, the reflection coefficients at 20 GHz are -0.9 dB and -0.65 dB for the unloaded and loaded cells respectively. The co-pol to cross-pol ratio for the RHCP waves with loaded cell has a 10 dB improvement at 20 GHz, while for the LHCP waves the performance is almost the same for both cells as expected. The only apparent disadvantage of loading is a slight reduction of BW-T bandwidth, which falls from 27.2% (5.44 GHz) to 23.3% (4.64 GHz). There is also a degradation of the RHCP transmission coefficient at high frequencies. It is clear however that this parameter is not the one limiting the bandwidth of the CPSS, as return losses under LHCP illumination are significantly higher.

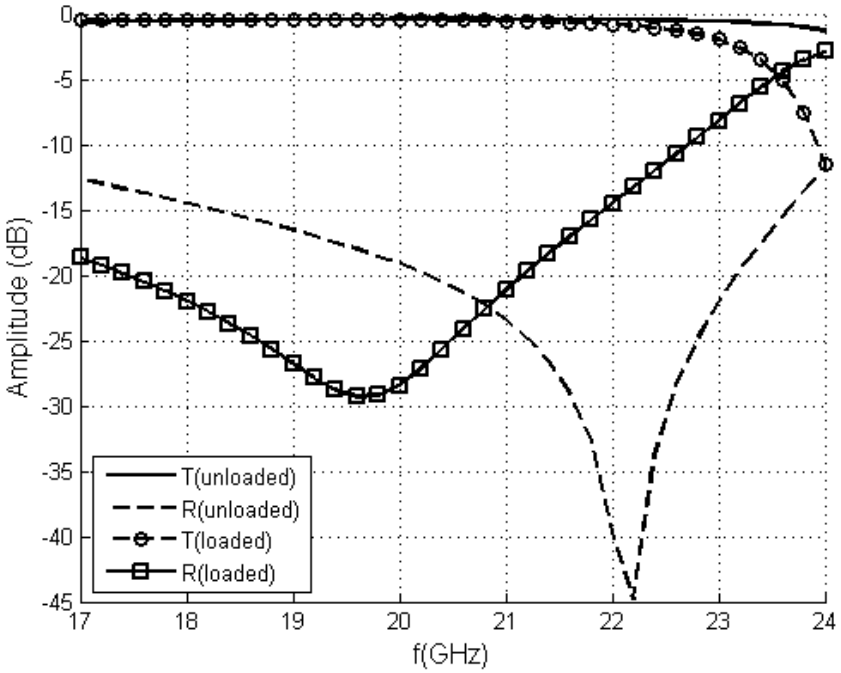

Figure 3.3: Comparison of the transmission and reflection coefficients for the RHCP waves for the unloaded and loaded Pierrot cell.

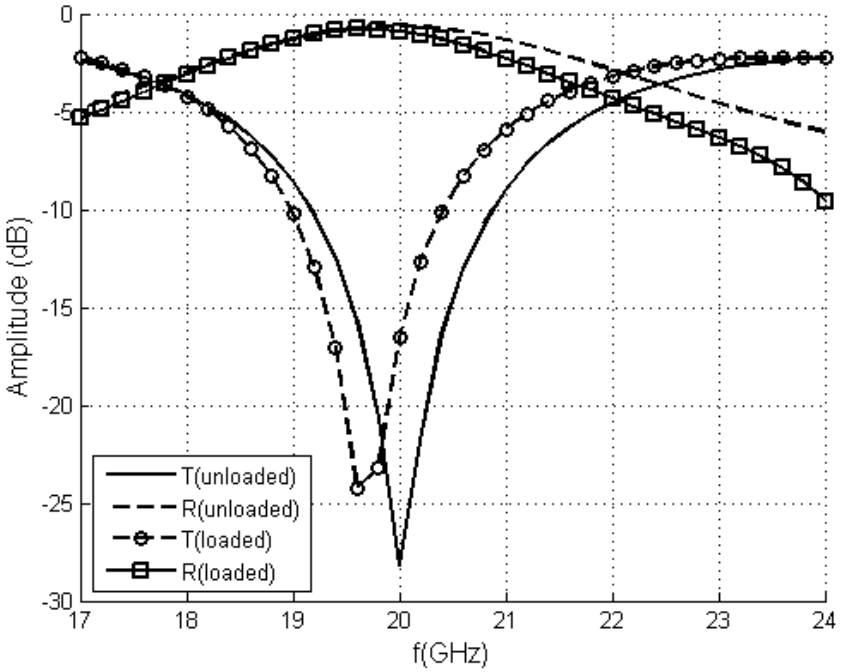

Figure 3.4: Comparison of the transmission and reflection coefficients for the LHCP waves for the unloaded and loaded Pierrot cell.

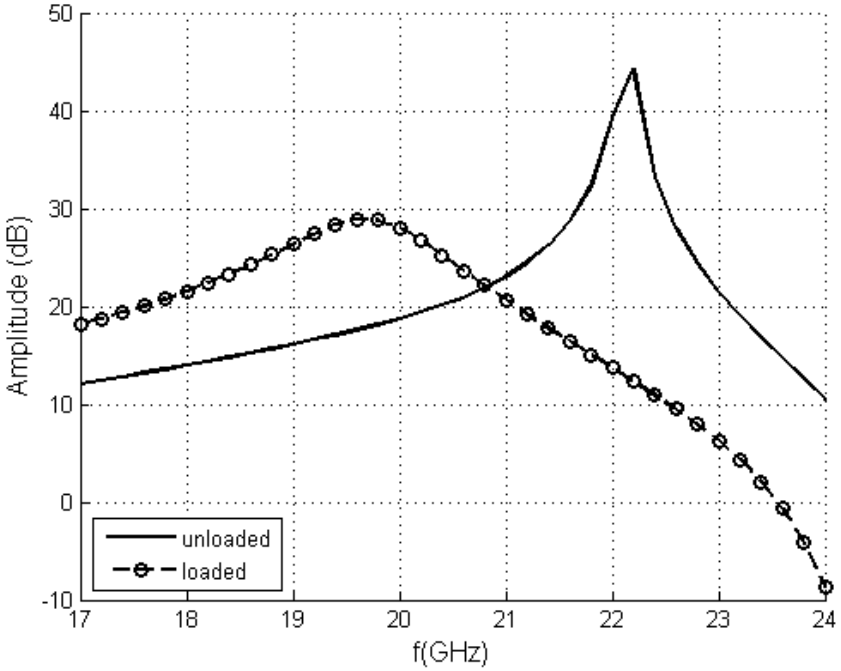

Figure 3.5: Comparison of the co-pol to cross-pol ratio for the RHCP waves for the unloaded and loaded Pierrot cell.

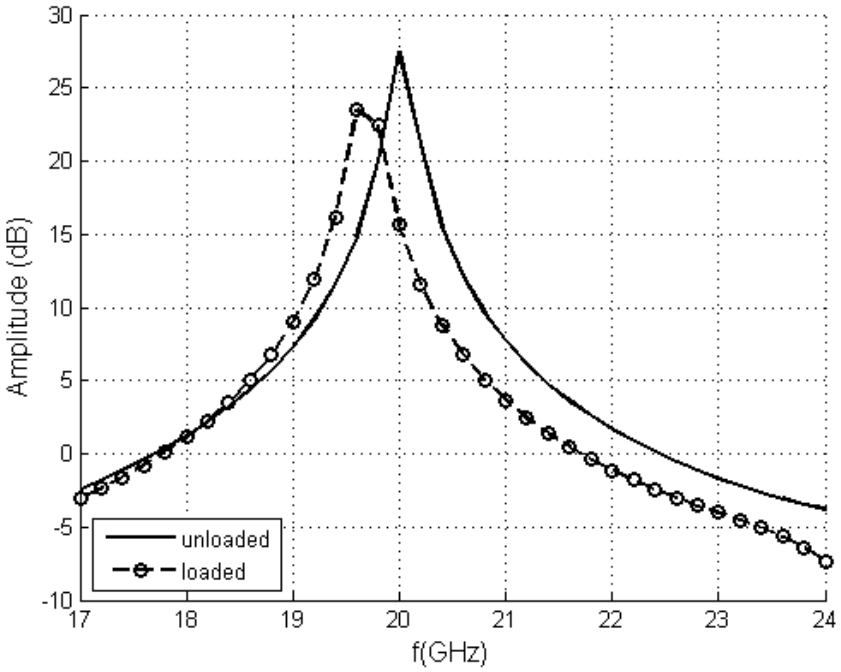

Figure 3.6: Comparison of the co-pol to cross-pol ratio for the LHCP waves for the unloaded and loaded Pierrot cell.

We have reduced the cross-polarization for both illuminations. In the next section we will study other variants of the Pierrot Cell to try to improve the performance of the CPSS, mainly the bandwidth.

3.3 Double Pierrot Cell variants

In Munk (2005) it is demonstrated that increasing the spatial density of cells in periodic frequency-selective surfaces leads to better bandwidths and less dependency of the performance on the incidence direction. In Roy (1995) it is also mentioned that unit cells having a 2-fold rotation symmetry lead to less performance degradation when the angle of incidence increases. In this section we are proposing a variant of the Pierrot cell-based CPSS. In comparison with the original "single crank" design shown in Fig. 1.4, the new design uses two cranks per unit cell in order to increase the density. In addition, the two cranks are in a spatial arrangement that has the desired 2-fold rotation symmetry. Once again, it will be observed that this implementation is greatly facilitated by the use of the newly proposed folded PCB fabrication approach.

3.3.1 Pierrot Cell at 90 degrees

In this section we will study a variant of the Pierrot cell that we call "Pierrot Cell at 90 degrees". This cell is illustrated in Fig. 3.7. Instead of being printed on the upper horizontal sections of the folded substrate, the upper segment is on the vertical wall and forms a 90 degree angle with the middle segment that is also on the vertical wall. The lower segment is perpendicular to the vertical wall which is not the case with the rest of the models used so far. The width of the horizontal segment is not the same as the width for the segments on the vertical wall. The goal of this model is to widen the bandwidth of the cell. This cell is designed for operation at 22 GHz in order to be able to integrate it in a double crank cell configuration. The objective of this configuration is to have two Pierrot cranks at different frequencies within the same unit cell, sharing the same height of the vertical walls in the substrate. Fig. 3.8 shows a 3D view of these two cells sharing the same substrate. A cell comprising only the proposed 90-degree crank will be analyzed before considering to integrate it in a double cell CPSS. The period of the cell is also 10 mm $\times$ 10 mm. As we did with the other models, the cell geometry was optimized. In this case, we used the equations in Table 3.1. After optimization, Table 3.3 shows the lengths of the segments.

Figs. 3.9 and 3.10 show respectively the transmission and reflection coefficients for the RHCP and LHCP waves for the simple unit cell shown in Fig. 2.5 and for the 90-degree cell, while Fig. 3.11 shows both the reflection and transmission AR for the same two cells. It

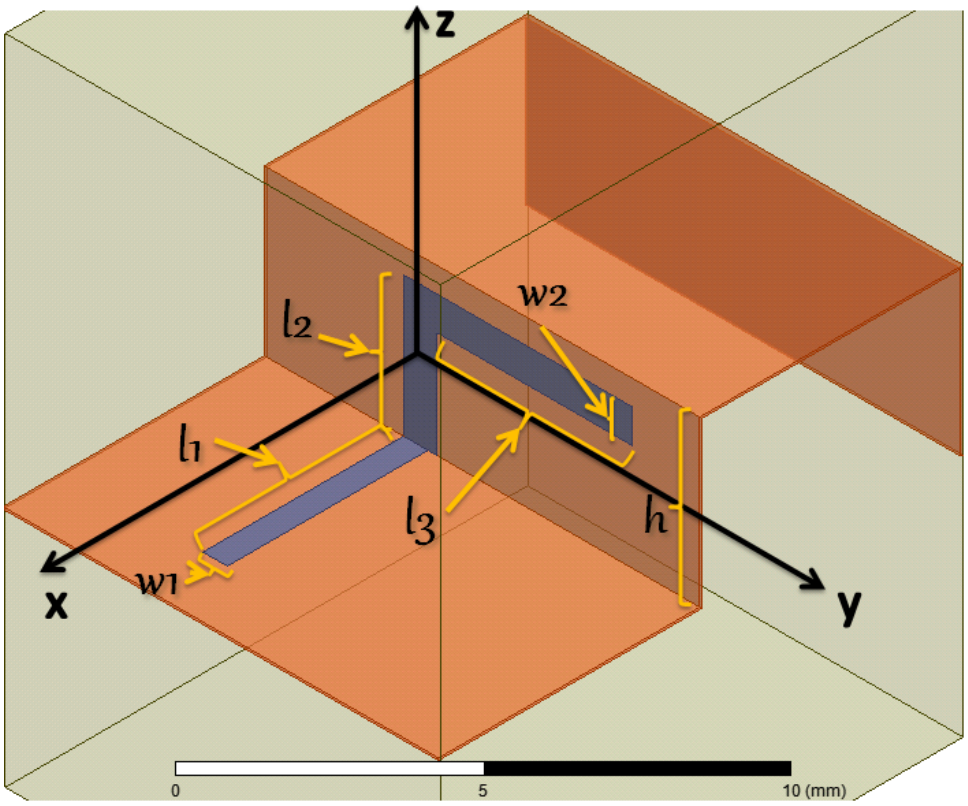

Figure 3.7: 3D model of the 90-degree Pierrot cell.

should be recalled that the simple unit cell was optimized for 20 GHz while the 90-degree cell is optimized at 22 GHz. From Fig. 3.9 we can see that b_r^{rR} is at -30 dB, which is very good. Transmission coefficients b_r^{tR} have very similar characteristics for the two CPSS's. Both of them are at around -0.5 dB. From Fig. 3.10, we can see the 90-degree cell has a 12% (2.65 GHz) BW-T bandwidth. In comparison, the simple unit cell had a 27% (5.44 GHz) BW-T bandwidth. We can see that the BW-T bandwidth is decreased considerably. And finally, from Fig. 3.11 we observe that the AR for the 90-degree cell is much deteriorated. So, this proposed cell will not be considered in the rest of this work as it did not provide an increase

Table 3.3: Physical characteristics of the 90-degree cell shown in Fig. 3.8 after optimization.

Period	10 mm × 10 mm
Length l_1 of horizontal segment on bottom horizontal wall	4.61 mm
Width w_1 of horizontal segment on bottom horizontal wall	0.77 mm
Height h of the vertical wall	3.78 mm
Width w_2 of the strips in the vertical wall	0.56 mm
Length $l_2$of the vertical segment in the vertical wall	3.21 mm
Length $l_3$of the horizontal segment in the vertical wall	4.49 mm

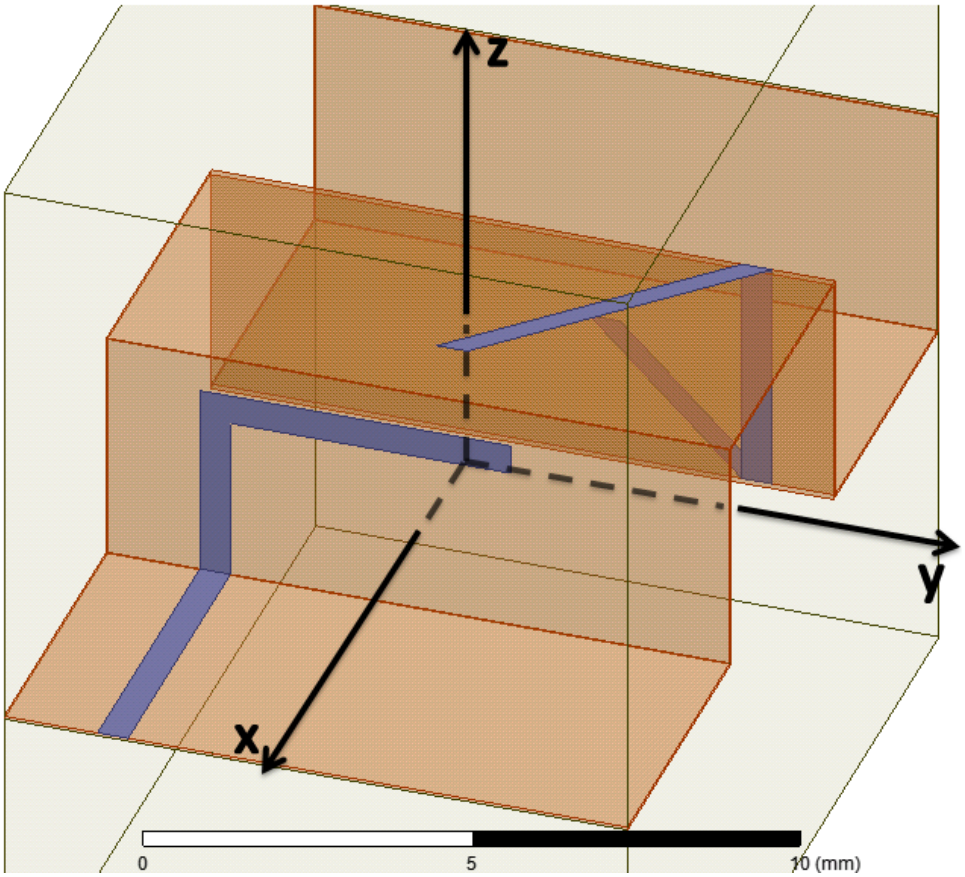

Figure 3.8: 3D view of the 90-degree Pierrot cell and a double Pierrot cell.

in performance in any case.

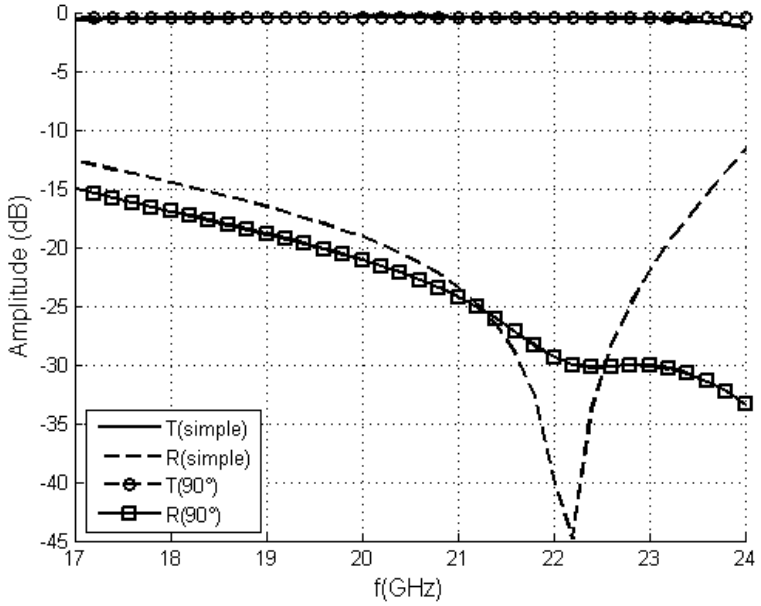

Figure 3.9: Comparison of the transmission and reflection coefficients for the RHCP waves for the simple Pierrot cell and the 90-degree cell.

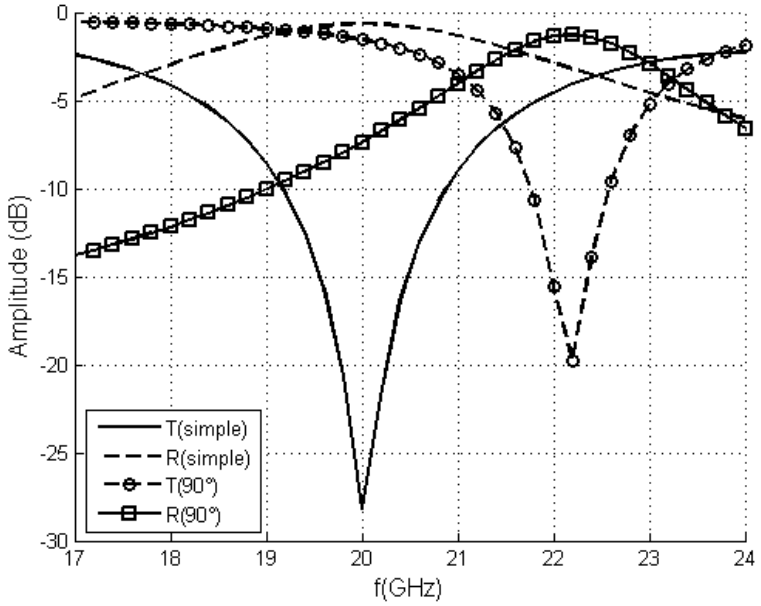

Figure 3.10: Comparison of the transmission and reflection coefficients for the LHCP waves for the simple Pierrot cell and the 90-degree cell.

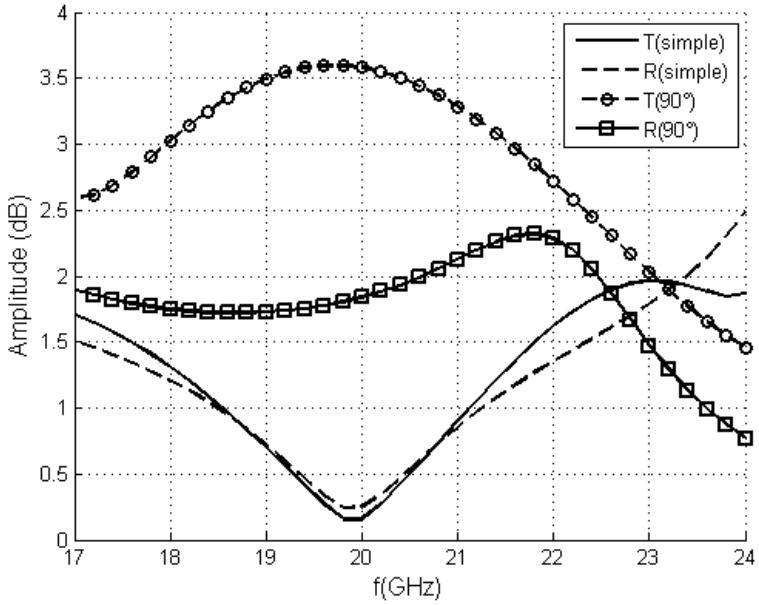

Figure 3.11: Comparison of the transmission and reflection AR for the simple Pierrot cell and the 90-degree cell.

3.3.2 Double Pierrot Cell at the same frequency

So far, the simple unit cell in Table 2.3 has the best performances of all the studied cells. In this section we will continue to focus on the bandwidth increase resulting from higher spatial density of cells. Also, we will focus on the effect of the incidence angle on the CPSS response. In order to reduce the dependence on the incidence angle on the reflection and transmission properties of the CPSS, it is desirable to have a two-fold rotational symmetry of the unit cell (see Roy and Shafai, 1996). Leveraging on the design flexibility of the printed CPSS structure, we propose a new double-Pierrot unit cell having such symmetry. Fig 3.12 shows a 3D view of this cell. Figs. 3.13 and 3.14 show the top view of a double cell and the lattice of cells respectively. We can see that the unit cell now consists in two identical cranks apart by 180 degrees around the z axis. The cell period is also 10 mm $\times$ 10 mm, as with the other CPSS studied so far. The lengths of the segments are also optimized with the same criteria as the simple unit cell. Table 3.4 shows the length of the segments after optimization.

Figs. 3.15 and 3.16 show comparisons of the simulation results for the simple and double crank Pierrot cells transmission and reflection coefficients for the RHCP and LHCP waves under normal incidence respectively. We observe that the double crank unit cell CPSS has a bandwidth BW-T of 23% (4.69 GHz) while the simple one had a bandwidth of 27%. The bandwidth has not increased but at 20 GHz, the double cell design offers a slight advantage

Table 3.4: Physical characteristics of the double crank Pierrot cell CPSS optimized with a period of 10 mm × 10 mm.

Period	10 mm × 10 mm
Horizontal segment length	5.19 mm
Vertical segment length	3.86 mm
Segments width	0.49 mm

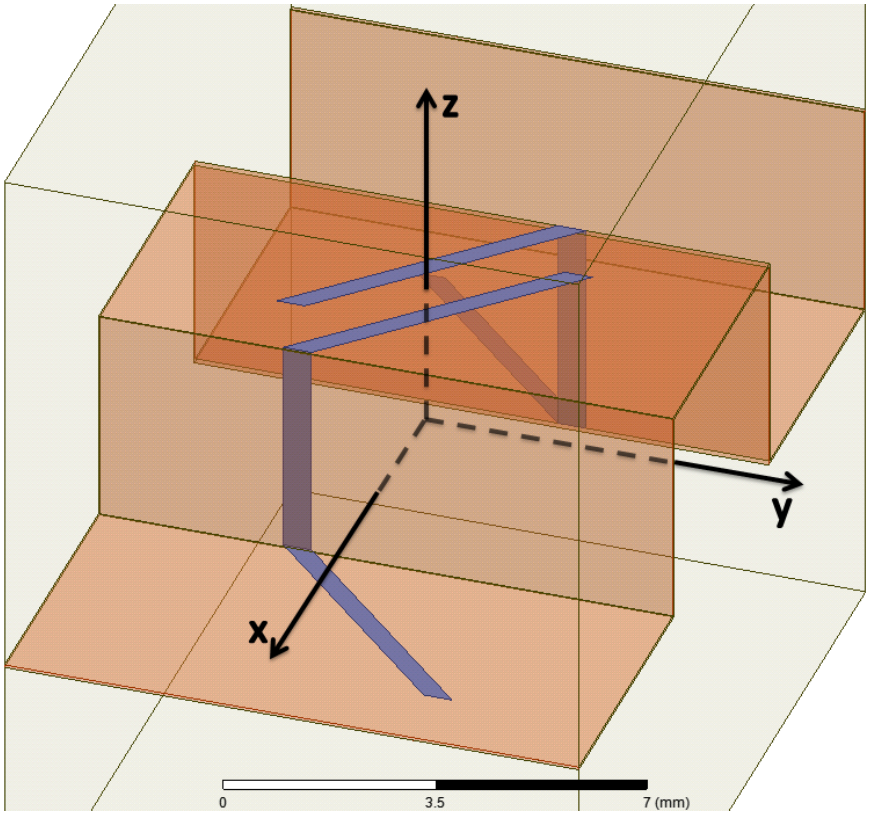

Figure 3.12: 3D model used to simulate the periodic structure of the double Pierrot Cell.

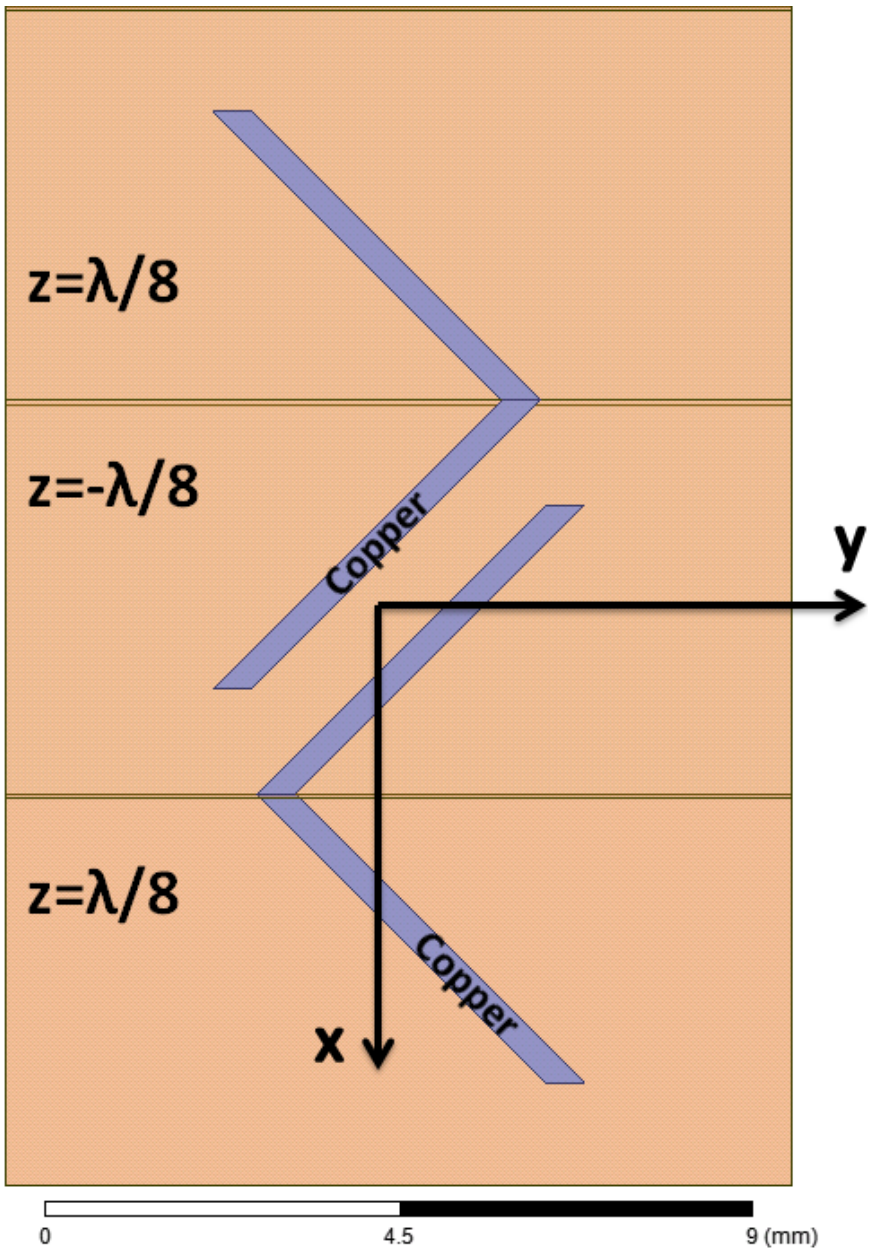

Figure 3.13: Top view of model of the double Pierrot Cell.

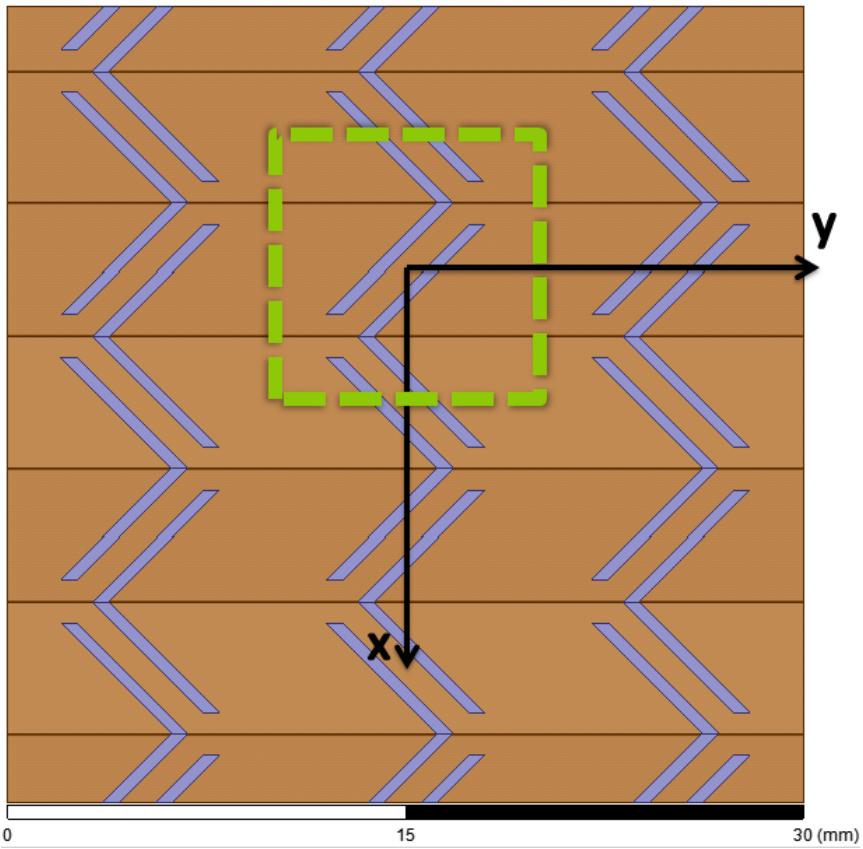

Figure 3.14: Periodic arrangement of the double Pierrot Cell having two-fold rotation symmetry around the z axis. The green rectangle outlines the boundaries of the unit cell simulated in HFSS.

over the simple one having a reflection coefficient for the LHCP waves at −0.96 dB versus −0.65 dB. Both CPSSs have similar transmission coefficients for the RHCP waves, −0.35 dB. The minimum of the reflection coefficient b_r^{rR} for the simple crank design is closer to the design frequency of 20 GHz. Fig. 3.17 shows a comparison of the simulation results of the variation of the transmission coefficient (b_l^{tL}) for the LHCP waves as a function of θ at the planes ϕ=45, 22.5 and 0 degrees at 20 GHz. We can see that the performance of the simple unit cell degrades more quickly than the double crank Pierrot cell, confirming the fact that a two-fold rotation symmetry diminishes quite significantly the dependency on the changes of the angle of incidence, as expected.

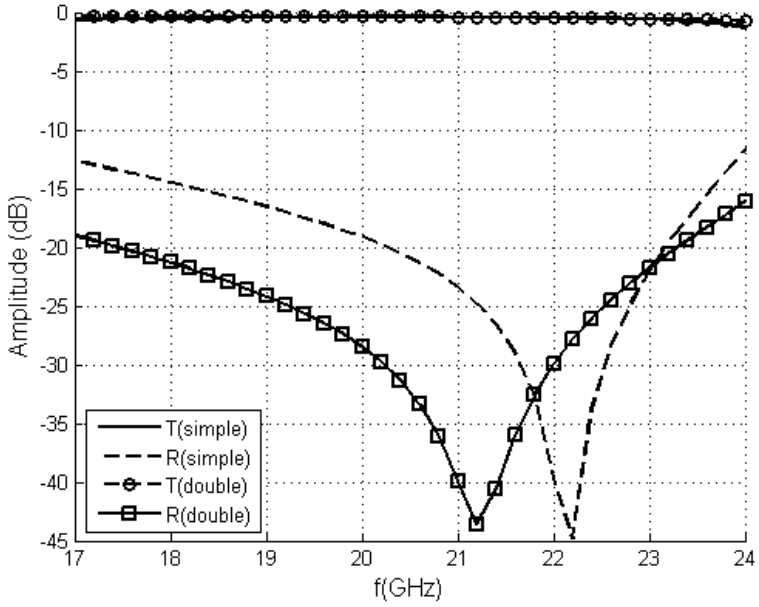

Figure 3.15: Comparison of the transmission (b_r^{tR}) and reflection (b_r^{rR}) coefficients for the simulated RHCP waves for the simple and double Pierrot cell.

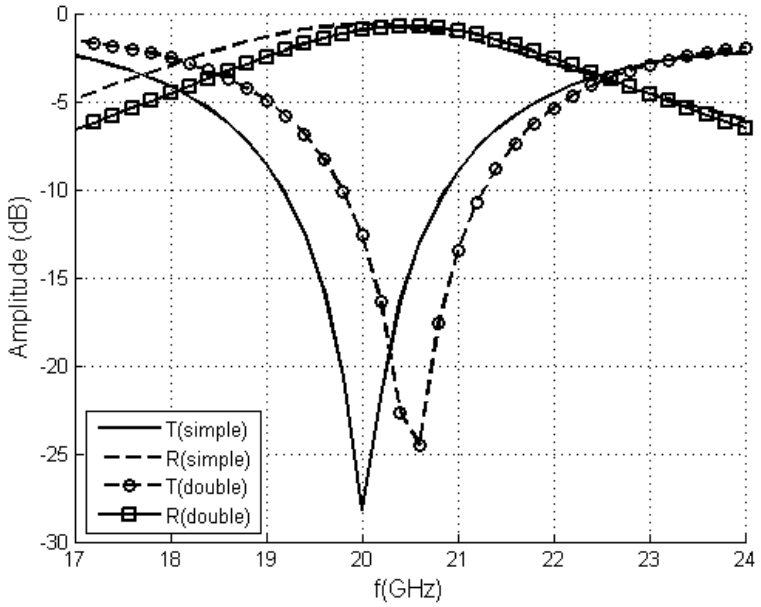

Figure 3.16: Comparison of the transmission (b_l^{tL}) and reflection (b_l^{rL}) coefficients for the simulated LHCP waves for the simple and double Pierrot cell.

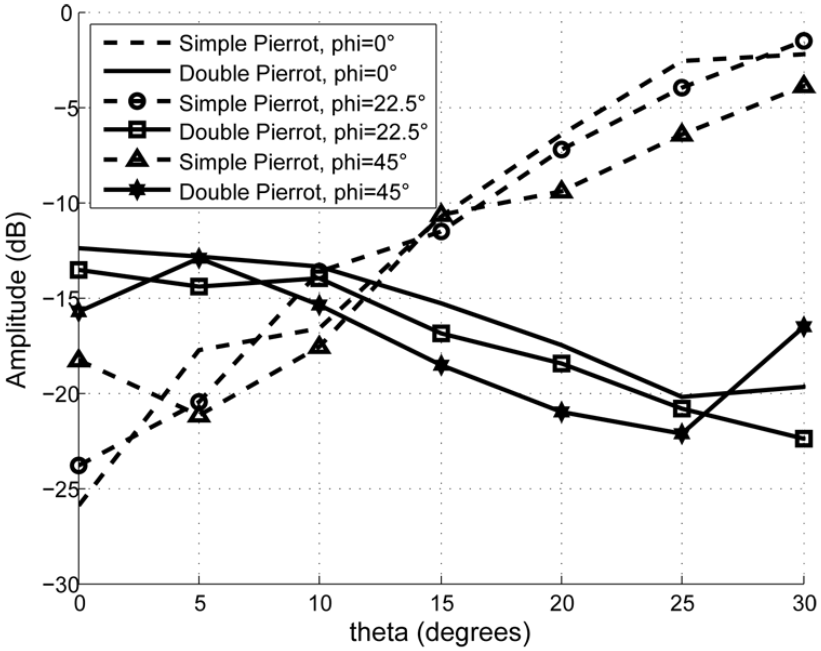

Figure 3.17: Simulated comparison of the variation of the transmission coefficient (b_l^{tL}) for the LHCP waves in function of θ at the planes ϕ=45, 22.5 and 0 degrees at 20 GHz for the simple and double crank designs. Both cells have period of 10 mm $\times$ 10 mm.

To increase even further the performance of the double crank Pierrot cell, we evaluated different cell periods (5 mm × 10 mm, 6 mm × 9 mm, 7 mm × 11 mm, 10 mm × 10 mm) to have a higher cell density. Each cell was optimized with the same criteria as above (see Table 3.4). Fig. 3.18 shows a comparison of the transmission coefficients b_l^{tL} under LHCP illumination for those periods. The cell with the period of 7 mm × 11 mm gives the best results with a BW-T bandwidth of 40% (increase of 17% compared to 23% of the 10 mm ×10 mm period cell) and minimum transmission coefficient b_l^{tL} (−28 dB) at 20 GHz. Table 3.4 shows the final dimensions of the segments after optimization.

Table 3.5: Physical characteristics of the double crank Pierrot cell CPSS optimized with a period of 7 mm × 11 mm.

Period	7 mm × 11 mm
Horizontal segment length	6.23 mm
Vertical segment length	3.57 mm
Segments width	0.45 mm

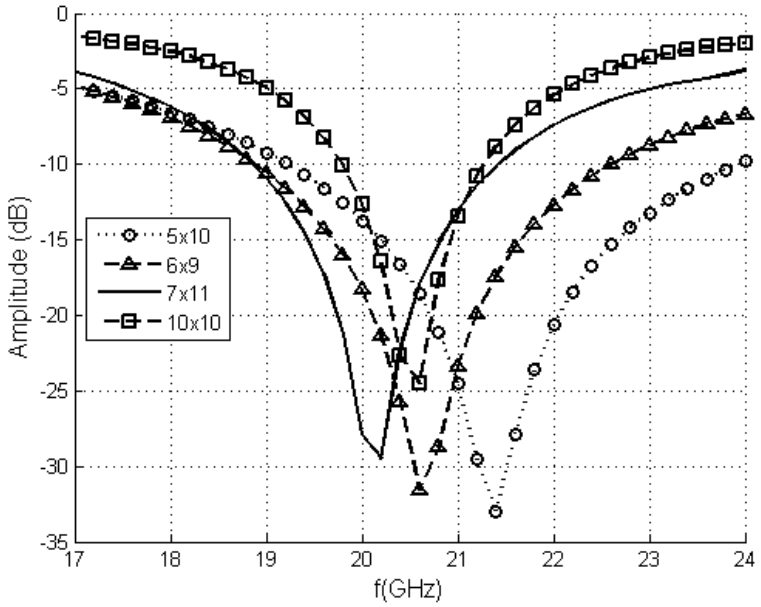

Figure 3.18: Comparison of the transmission coefficient (b_l^{tL}) of the LHCP waves for the double Pierrot cell with different periods.

Fig 3.19 shows a comparison of the transmission coefficient b_r^{tR} under RHCP illumination for the simple Pierrot cell, double Pierrot cell with period of 10 mm × 10 mm and double Pierrot cell with period of 7 mm × 11 mm. All the cells have a transmission coefficient b_r^{tR} at around −0.4 dB. At higher frequencies, it is the double crank Pierrot cell with a period

of 7 mm × 11 mm that degrades more rapidly. This behavior at higher frequencies has been observed in other CPSS as well (see Tarn and Chung, 2007). Fig. 3.20 shows a comparison of the transmission coefficient b_l^{tL} under LHCP illumination for the three cells mentioned above. We observe a BW-T bandwidth increase of 17% (40%, 8.1 GHz) compared to 23% (4.69 GHz) of the 10 mm ×10 mm period cell and 27% (5.44 GHz) of the simple unit cell. Fig. 3.21 shows a comparison of the reflection coefficient b_l^{rL} under LHCP illumination for the same three cells. We observe a BW-T bandwidth increase of 10% (30%, 6.14 GHz) compared to 17% (3.48 GHz) of the 10 mm ×10 mm period cell and 20% (4.11 GHz) of the simple unit cell. This confirm that with a higher cell density, the bandwidth is increased considerably (see Munk, 2005). Fig. 3.22 shows the co-pol to cross-pol ratio of the transmitted wave in the case of RHCP incidence, also for the three cells mentioned above. Here, it is the double cell with a period of 7 mm × 11 mm that gives the best result at the design frequency. In terms of the transmission AR (see Fig. 3.23), it is the double cell with period of 7 mm × 11 mm that has the largest B-AR$_t$, although the lowest value of 0.29 dB is at 20.38 GHz while the lowest for the simple and double cell with period of 10 mm × 10 mm are at 20 and 19 GHz (0.24 dB and 0.15 dB) respectively. Table 3.6 resumes the simulation results for these three cells.

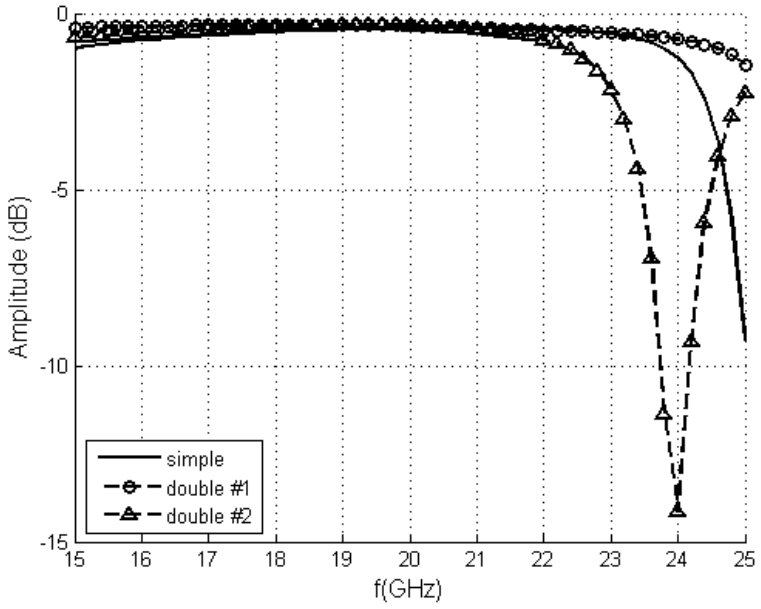

Figure 3.19: Comparison of the transmission of the RHCP waves for the simple Pierrot cell, double Pierrot cell with period of 10 mm × 10 mm (#1) and double Pierrot cell with period of 7 mm × 11 mm (#2).

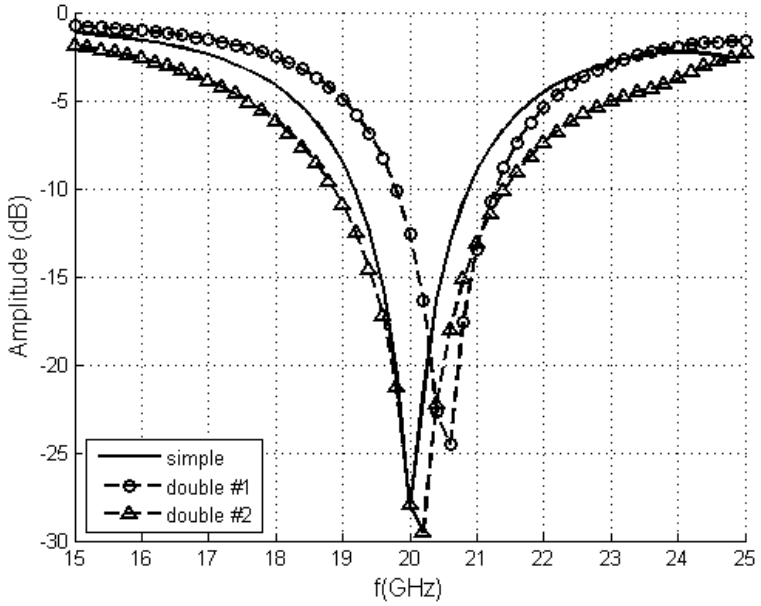

Figure 3.20: Comparison of the transmission of the LHCP waves for the simple Pierrot cell, double Pierrot cell with period of 10 mm × 10 mm (#1) and double Pierrot cell with period of 7 mm × 11 mm (#2).

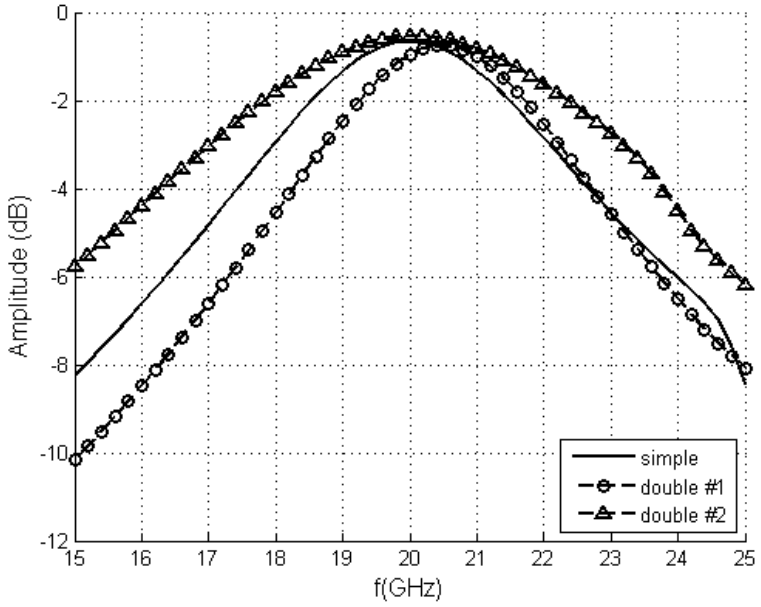

Figure 3.21: Comparison of the reflection of the LHCP waves for the simple Pierrot cell, double Pierrot cell with period of 10 mm × 10 mm (#1) and double Pierrot cell with period of 7 mm × 11 mm (#2).

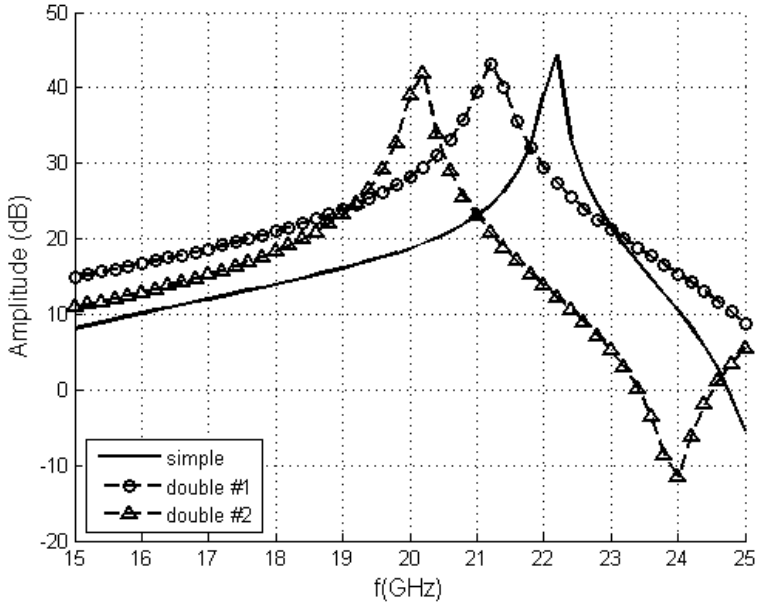

Figure 3.22: Comparison of the co-pol to cross-pol ratio of the RHCP waves for the simple Pierrot cell, double Pierrot cell with period of 10 mm × 10 mm (#1) and double Pierrot cell with period of 7 mm × 11 mm (#2).

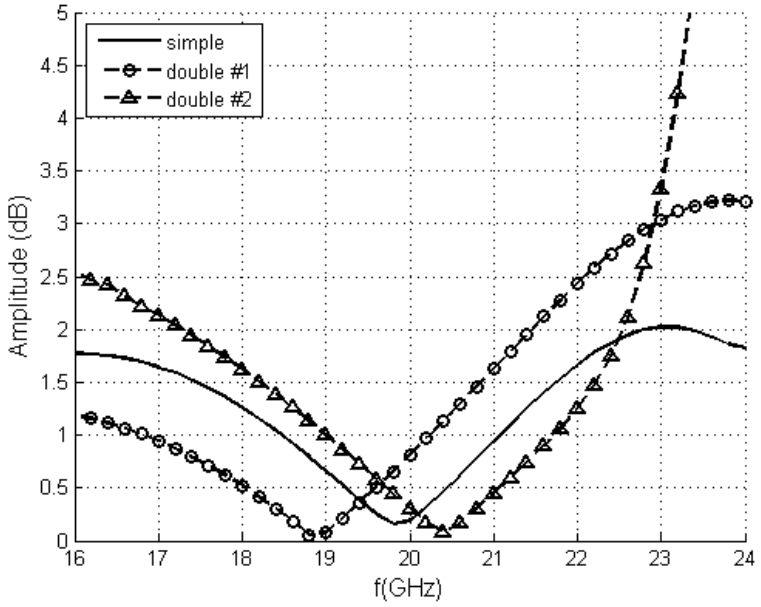

Figure 3.23: Comparison of the transmission AR for the simple Pierrot cell, double Pierrot cell with period of 10 mm × 10 mm (#1) and double Pierrot cell with period of 7 mm × 11 mm (#2).

Table 3.6: Simulation results for the simple Pierrot cell, double Pierrot cell with period of 10 mm × 10 mm (#1) and double Pierrot cell with period of 7 mm × 11 mm (#2).

Cell	BW-T (%)	BW-R (%)	AR_t (dB) @ 20 GHz	B-AR_t (GHz)
Simple	27%	20%	0.24	18.49-21.26
Double #1	23%	17%	0.81	16.8-20.26
Double #2	40%	30%	0.33	19.03-21.87

3.3.3 Double Pierrot Cell at two frequencies

In this section, we study one last approach to try to increase the bandwidth of the CPSS. The approach used here is similar to that used in broadband antennas, in which increase of bandwidth can be obtained by concatenating elements having slightly different resonance frequencies (as for instance in a log-periodic dipole array). As a first attempt in this direction, and as mentioned in the section 3.3.1, we propose a unit cell comprising two Pierrot crank elements, each crank having circular polarization selectivity at a different frequency. The difficulty with this approach is that as illustrated in Fig. 1.4, each crank should have a vertical segment of length $\lambda/4$. If the two cells are implemented with the folded PCB approach proposed in Chapter 2, we have the physical constraint that both cells share the same height in the vertical segment height. One possibility to circumvent this problem is to vary the angle between the two horizontal segments. In this way, we shorten (or widen, depending on the case) the distance needed for the RH and LH electrical fields to be tangential with the horizontal segments of the CPSS at the same time, therefore causing a resonance. For the CPSS in section 3.3.2, this angle is always 90 degrees and it will be our reference for the other cells operating at different frequencies. We tested three design frequencies in addition to a 20 GHz CPSS, 18, 19 and 21 GHz. We will illustrate the calculation of the angle with the cell operating at 18 GHz. We know that

$$\frac{\lambda}{4} \Longleftrightarrow 90\,\text{degrees}$$

We can find the equivalent distance at 18 GHz of a distance of $\lambda/4$ at 20 GHz

$$0.25 \times \frac{18}{20} = 0.225$$

By the rule of three

$$\begin{aligned} 0.25 &\longrightarrow 90 \\ 0.225 &\longrightarrow X \end{aligned}$$

So we can find the angle as

$$X = 90 \times \frac{0.225}{0.25} = 81$$

Table 3.7 shows the angle between the horizontal segments and the design frequency. Figs 3.24 and 3.25 show respectively a 3D view and top view of the cell operating at 18 and 20 GHz. The period for all the cells in this section is 7 mm × 11 mm, which is the same period of the cell in Table 3.5. To optimize each cell, we start with the design of the double crank Pierrot cell considered in the last section which was optimized for 20 GHz with the criteria in Table 3.1. Then, keeping the same height in the vertical segment, we adjust each new cell at the corresponding angle between the horizontal segments. After doing this, we optimize again with the same criteria by only changing length of the horizontal segments and width of all the segments of the cell not running at 20GHz. Tables 3.8 to 3.11 show the dimensions of each cell after the whole optimization process.

Table 3.7: Angle between the horizontal segments according to the design frequency for the CPSSs at two frequencies.

Design frequency	Angle between horizontal segments
18 GHz	81 degrees
19 GHz	85.5 degrees
20 GHz	90 degrees
21 GHz	94.5 degrees

Table 3.8: Physical characteristics of the double crank Pierrot cell CPSS optimized at 18 and 20 GHz.

	18 GHz	20 GHz
Period	7 mm × 11 mm	
Vertical segment length	3.57 mm	
Horizontal segment length	6.05 mm	6.23 mm
Segments width	0.49 mm	0.45 mm

Figs. 3.26 and 3.27 show the results for the transmission coefficients for the RHCP and LHCP waves for the four cells described above, while Fig. 3.28 shows the reflection coefficients for the LHCP waves. We observe that the transmission coefficients for the RHCP waves for all the cells are around −0.4 dB. However, these coefficients drop considerably after 22 GHz, as observed also in Fig. 3.19. In terms of the LHCP waves, there is a slight increment in the BW-T and BW-R bandwidths in comparison to the cell operating only at 20 GHz. Fig. 3.29 shows the transmission AR for these cells. In this case, the best AR results have shifted to other frequencies. The cell operating at 21 and 20 GHz has its results more centered on

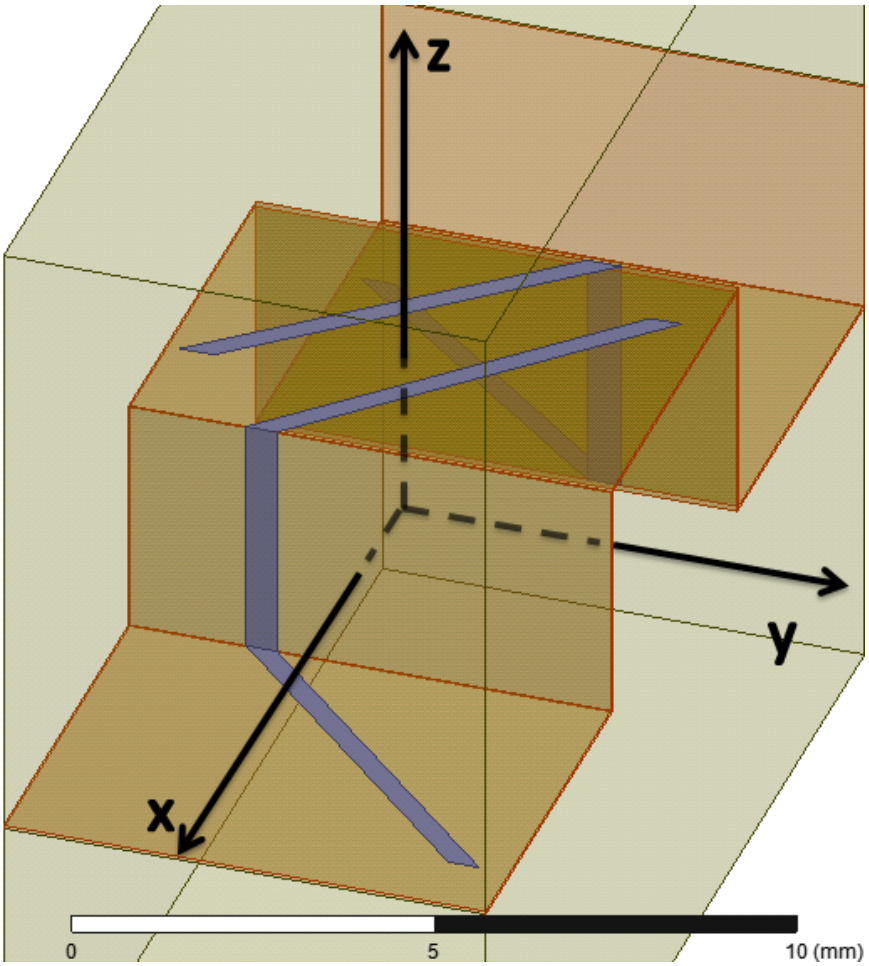

Figure 3.24: 3D model used to simulate the periodic structure of the double Pierrot Cell at 18 and 20 GHz.

Table 3.9: Physical characteristics of the double crank Pierrot cell CPSS optimized at 19 and 20 GHz.

	19 GHz	20 GHz
Period	7 mm × 11 mm	
Vertical segment length	3.57 mm	
Horizontal segment length	5.92 mm	6.23 mm
Segments width	0.51 mm	0.45 mm

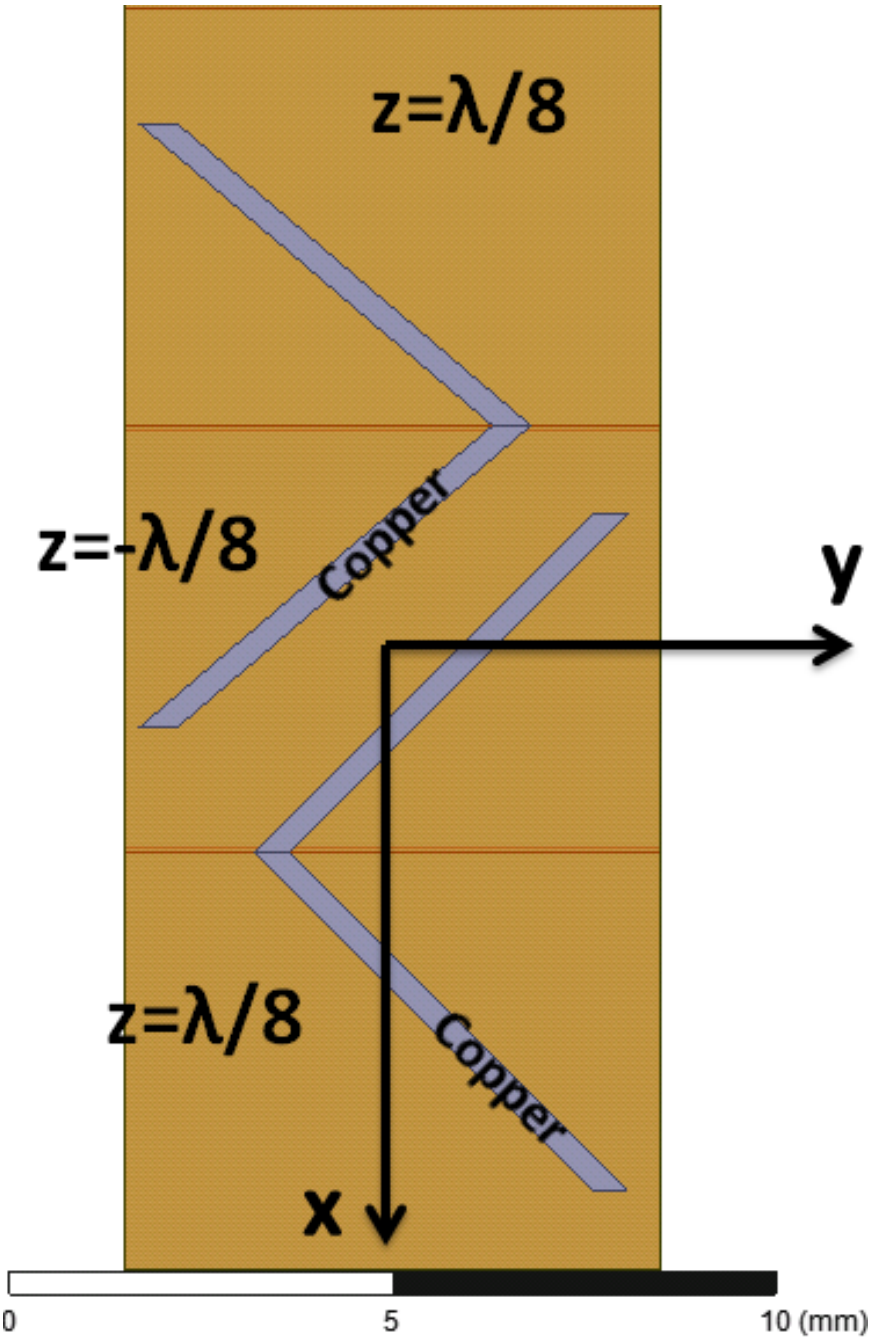

Figure 3.25: Top view of model of the double Pierrot Cell at 18 and 20 GHz.

Table 3.10: Physical characteristics of the double crank Pierrot cell CPSS optimized at 20 GHz.

Period	7 mm × 11 mm
Vertical segment length	3.57 mm
Horizontal segment length	6.23 mm
Segments width	0.45 mm

Table 3.11: Physical characteristics of the double crank Pierrot cell CPSS optimized at 21 and 20 GHz.

	21 GHz	20 GHz
Period	7 mm × 11 mm	
Vertical segment length	3.57 mm	
Horizontal segment length	5.87 mm	6.23 mm
Segments width	0.69 mm	0.45 mm

the frequency of design, but the B-AR$_t$ is not the best of all the cases. The cell operating only at 20 GHz gives the best B-AR$_t$ in the band of 19.03-21.87 GHz. Fig. 3.29 shows a comparison of the co-pol to cross-pol ratio of the RHCP waves for these cells as well. All the configurations have similar ratios having a decent cross-polarization performance. Table 3.12 shows a comparison of the BW-T and BW-R bandwidths and transmission AR at 20 GHz for the double crank Pierrot cells operating at different frequencies and the simple unit cell from Chapter 2. Even if the bandwidth has been increased, the AR has a slight degradation in the cells operating at two different frequencies.

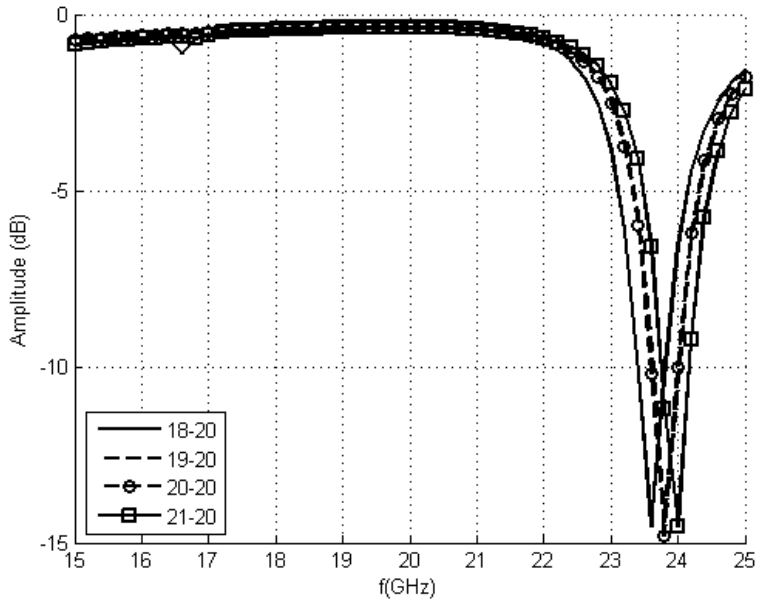

Figure 3.26: Comparison of the transmission of the RHCP waves for the double Pierrot cells designed for different pairs of frequencies.

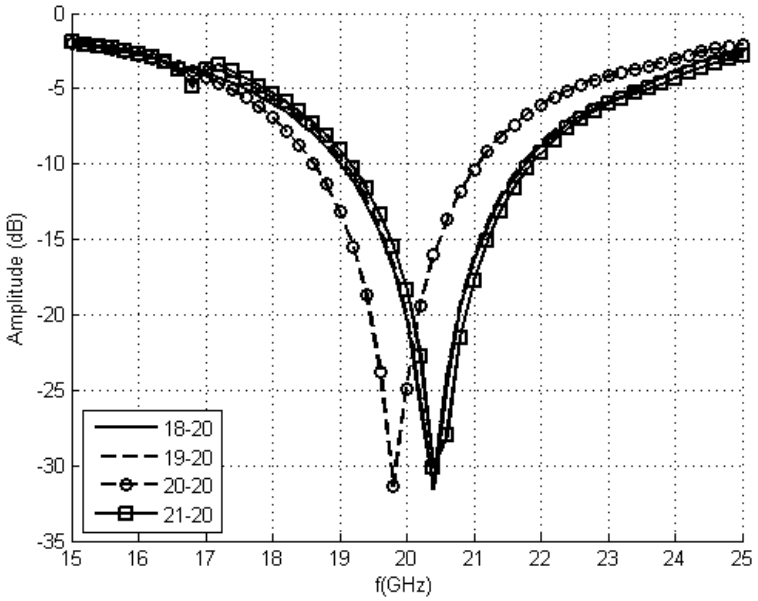

Figure 3.27: Comparison of the transmission of the LHCP waves for the double Pierrot cells designed for different pairs of frequencies.

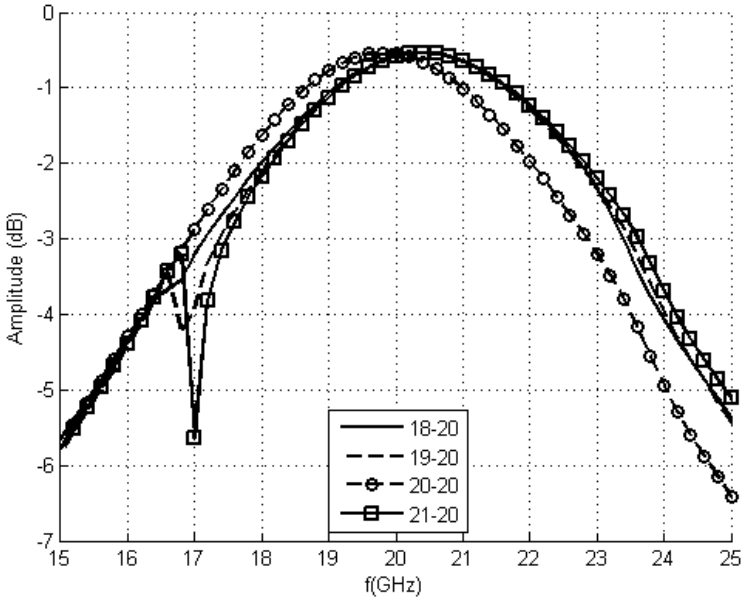

Figure 3.28: Comparison of the reflection of the LHCP waves for the double Pierrot cells designed for different pairs of frequencies.

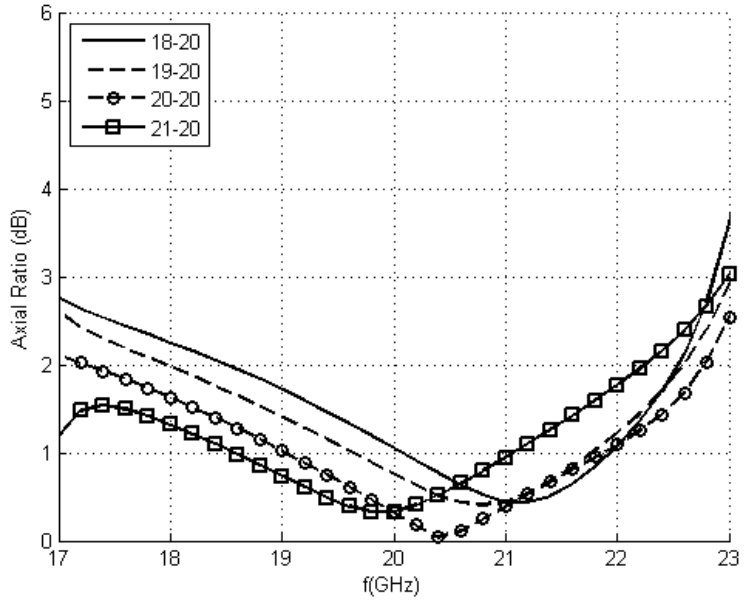

Figure 3.29: Comparison of the transmission AR for the double Pierrot cells designed for different pairs of frequencies.

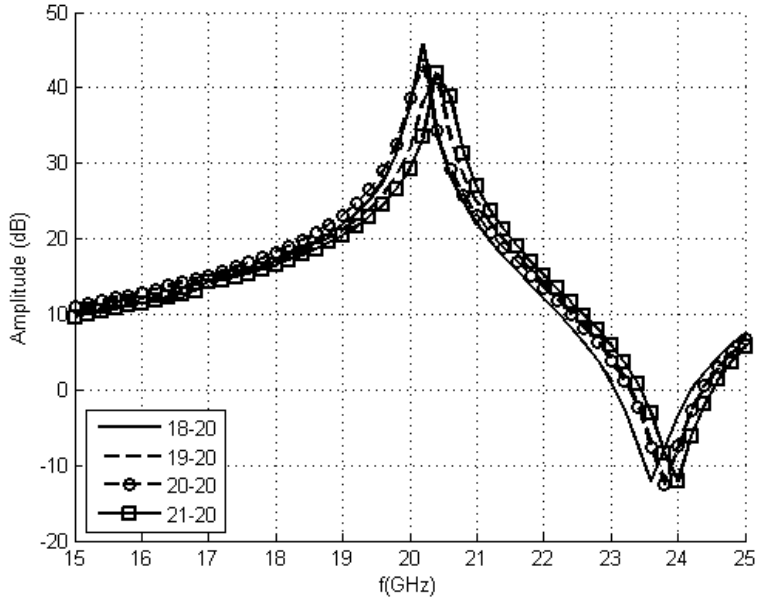

Figure 3.30: Comparison of the co-pol to cross-pol ratio of the RHCP waves for the double Pierrot cells designed for different pairs of frequencies.

Table 3.12: BW-T and BW-R bandwidths and transmission AR for the double crank Pierrot cells operating at different frequencies and the simple unit cell.

Cell	BW-T (%)	BW-R (%)	AR_t (dB) @ 20 GHz	B-AR_t (GHz)
18-20	41.7	31.2	1.05	20.07-21.94
19-20	41.7	30.5	0.75	19.63-21.78
20-20	40.0	29.7	0.33	19.03-21.87
21-20	43.1	30.6	0.33	18.57-21.07
Simple unit	27.0	20.5	0.15	18.46-21.08

3.3.4 Double Pierrot Cell Prototypes

In order to validate the double crank Pierrot cell we are proposing in this work, we fabricated a prototype with the dimensions given in Table 3.5 and with the procedure described in Section 2.4. We chose this cell for fabrication because it has a very good bandwidth of 40% while keeping its maximum of co-pol to cross-pol ratio very close to 20 GHz and having a good performance in terms of the transmission AR. We characterized this new prototype with the test bench described in Section 2.4. Fig. 3.31 shows a comparison of the transmission coefficients for this prototype and the prototype in Table 2.3.

The double crank Pierrot cell CPSS offers a bandwidth increase of 15.4% (33% versus 17.6%) which is in good agreement with the simulations. The transmission coefficient at the design frequency of 20 GHz for the RHCP waves are -0.3 dB and -0.55 dB for the double and simple unit Pierrot cells respectively. Fig. 3.32 shows a comparison of the variation of the transmission coefficient b_l^{tL} for LHCP illumination as a function of θ at 20 GHz for the fabricated prototypes and the simulated results. These results are in the plane $\phi = 45$ degrees which is the main plane of the CPSS as described in section 2.2. Here we can also confirm that the double crank Pierrot cell is less sensitive to variations of the angle of incidence. The transmission coefficients for the LHCP waves at 20 degrees for the double Pierrot cell have increased from -13.5 dB to -7 dB while the coefficients for the simple Pierrot cell have increased from -13.5 dB to -3 dB.

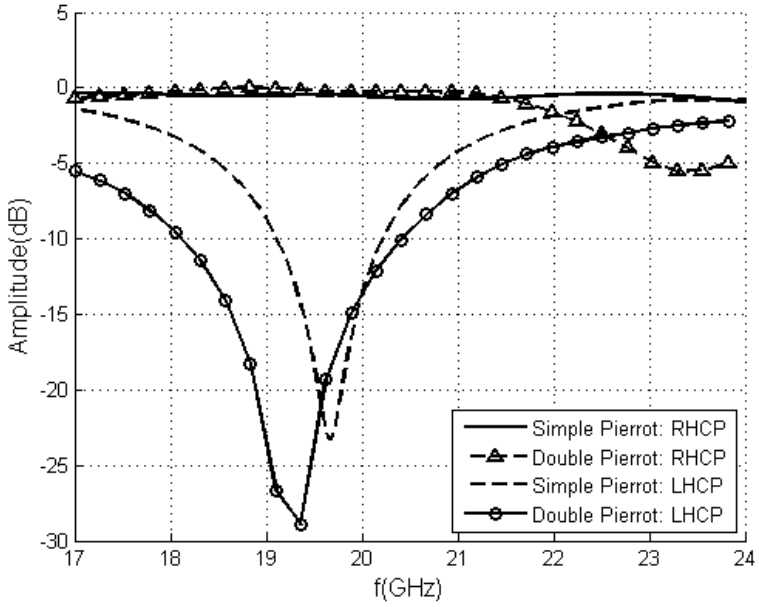

Figure 3.31: Comparison of the measurements of the transmission coefficients of the simple and double Pierrot cell fabricated prototypes under normal incidence.

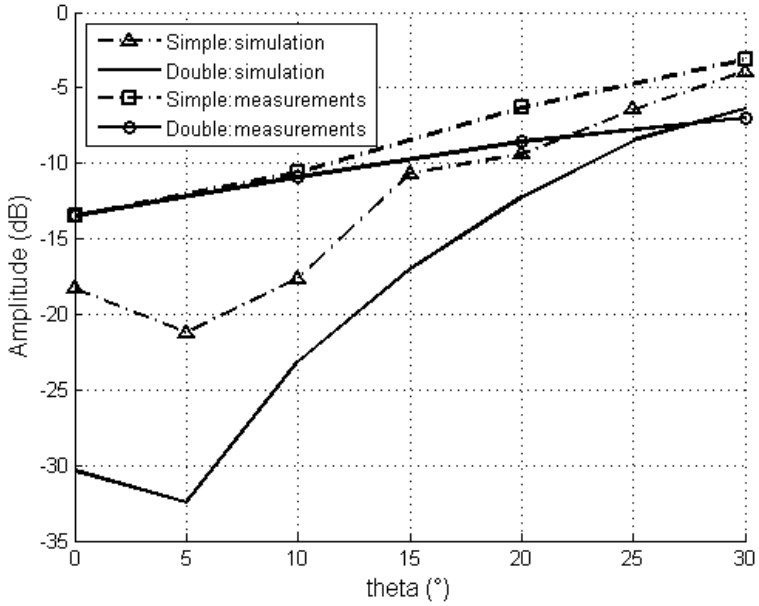

Figure 3.32: Comparison of the variation of the transmission coefficients for the LHCP waves as a function of θ in the plane ϕ=45 degrees at 20 GHz for the simple and double Pierrot cell, for the simulated and measured results.

3.4 Impact of the Foam substrate properties on the performance of the CPSS

At the design frequency of 20 GHz considered in this work, the electrical properties of the rohacell foam used in the fabricated CPSS are, as it can be realized from the high value of loss tangent, mainly suspected as an important cause of losses in the CPSS. In order to verify this, and at the same time to improve the performance of the CPSS, we have studied two modifications to the original foam support for the simple unit cell CPSS. The first modification simply consists in a reduction of the foam layer thickness, but the overall structure of the CPSS is the same as in Fig. 2.5. The thickness of the foam under the lower substrate level and above the upper substrate level is reduced from 5.5 mm to 1 mm. Note that this reduced thickness will decrease the mechanical stiffness, which may or may not be acceptable depending on the application. For the second modification, square holes are machined in the existing foam in the areas where the metallic Pierrot cell are printed. The objective of this modification is to remove lossy foam in regions where the electric field is more highly concentrated, while keeping it in other regions to preserve the mechanical integrity of the CPSS. Fig. 3.33 shows the top view of this model. The thickness of the foam above the top substrate level and below the bottom substrate level remains at 5.5 mm. The holes are rectangles of dimensions 8.5 mm $\times$ 5.75 mm.

Figs. 3.34 and 3.35 show a comparison of the simulated results for the transmission coefficient b_r^{tR} under RHCP illumination and the reflection coefficient b_l^{rL} under LHCP illumination for the original model and the two modified models respectively. We observe that with both thinner and perforated foams, the transmission coefficient for the RHCP waves increases by 0.2 dB (from -0.4 dB to -0.2 dB). In the case of perforated foam, the reflection coefficient of the LHCP waves increases by 0.37 dB (from -0.65 dB to -0.28 dB) at the design frequency. The benefit of using a thinner foam layer on this reflection coefficient is however marginal. These differences of behavior between the two polarizations can be understood by considering the current distribution on the one-wavelength long trace forming Pierrot cell. In the case of RHCP illumination, the trace is in anti-resonance and its current is very low. When the incident wave is LHCP the trace resonates with strong currents in phase opposition on its two halves. These stronger currents cause E field hot spots near the traces. Therefore removing lossy foam from this region leads to lower return losses. A support with holes was fabricated for the same CPSS described above. Fig. 3.36 shows a close view of 12 cells of the fabricated prototype. The dimensions of the finished CPSS are 20 cm $\times$ 20 cm $\times$ 2.192 cm and the number of cells is 20 by 19. Fig. 3.37 shows a comparison of the measurements results of the fabricated prototypes (thick foam and foam with holes) for the transmission coefficients of the RHCP and LHCP waves. These results confirm that with less foam, the losses in the

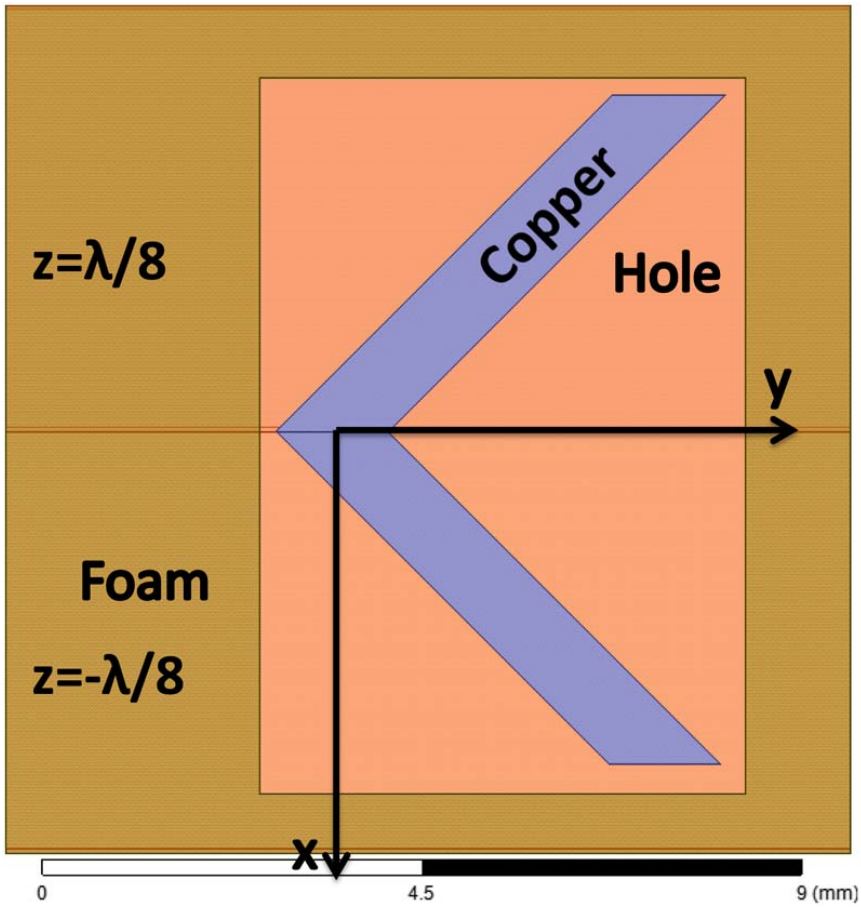

Figure 3.33: Top view of the model of the simple Pierrot Cell with square holes in the foam.

system are less significant, increasing the RHCP transmission coefficient by 0.4 dB (−0.5 dB to −0.1 dB) at 20 GHz.

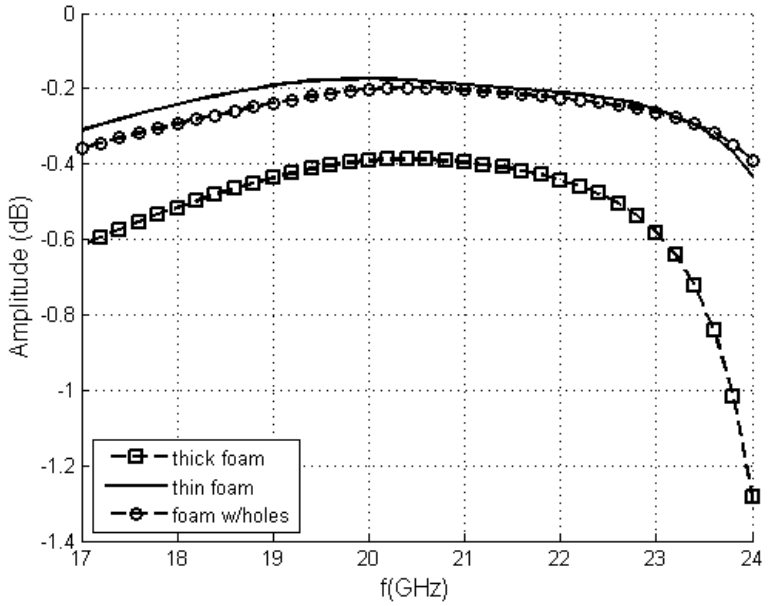

Figure 3.34: Comparison of the transmission coefficient for the RHCP waves for the simple Pierrot cell with different foam support configurations.

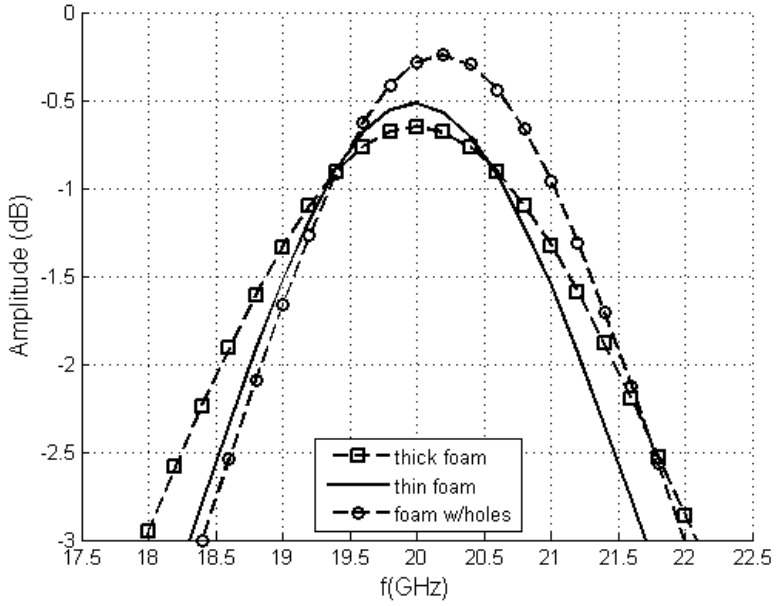

Figure 3.35: Comparison of the reflection coefficient for the LHCP waves for the simple Pierrot cell with different foam support configurations.

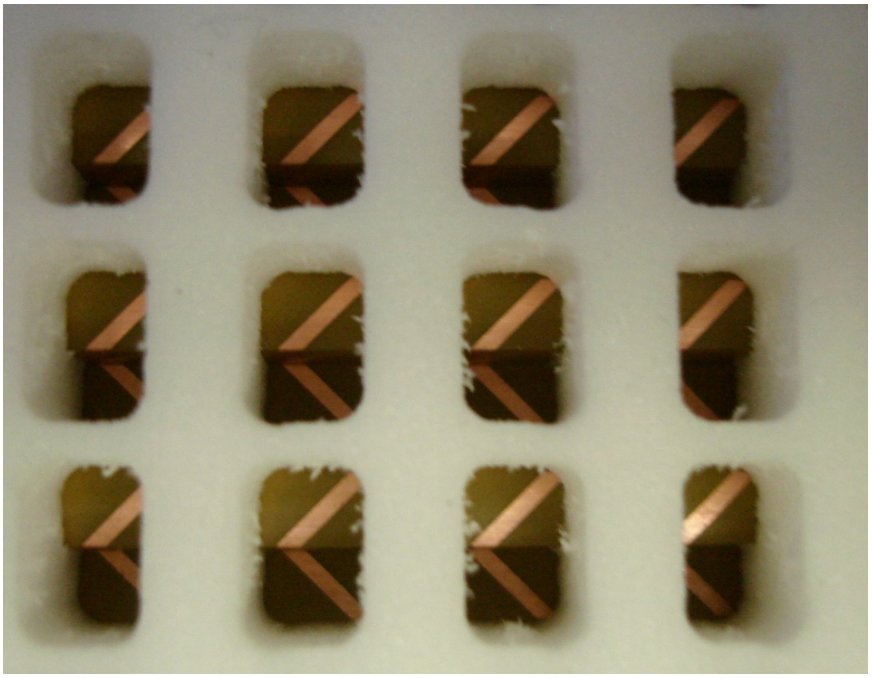

Figure 3.36: Close view of the fabricated prototype with holes in the foam support.

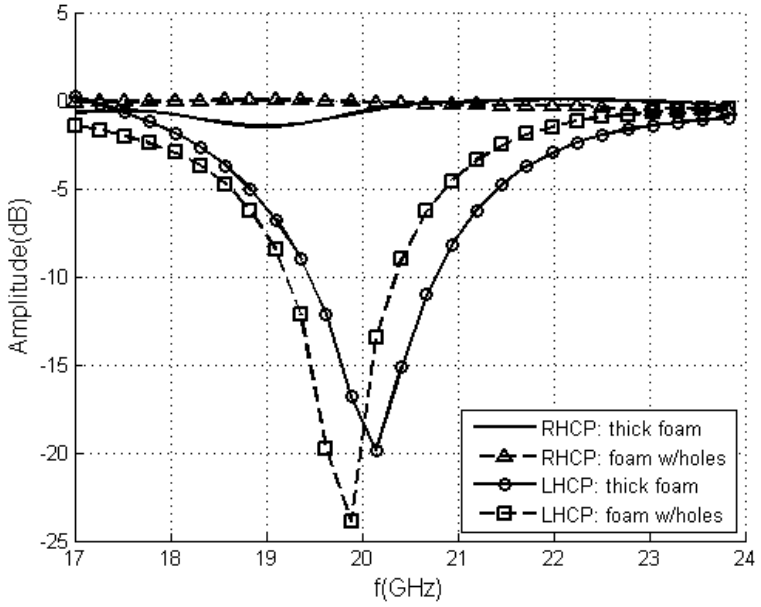

Figure 3.37: Comparison of the measurements results of the transmission coefficients of the RHCP and LHCP waves of the fabricated prototypes with thick foam and foam with holes.

CHAPTER 4

CONCLUSIONS

4.1 Thesis Contributions

With a CPSS, it is possible to accommodate multiple polarizations in the same antenna aperture, thus reducing the weight and volume of antennas used in satellites. Future broadband systems operating in the K and Ka bands will require circular polarization. This project focused on new types of CPSS based on the Pierrot unit cell using standard printed circuit fabrication techniques. This new approach permits a lot of freedom to design a CPSS on the PCB making it very easy to fabricate cells that do not have the typical structure of the Pierrot cell as showed in Fig. 1.4 while keeping or improving the performance of the CPSS. This technique uses a folded flexible substrate which enables the implementation in a single metal layer.

We started with a simple unit cell designed on a thin flexible substrate. A foam support was also designed to give support to the structure. A prototype was fabricated and characterized. At 20 GHz, the measured LHCP and RHCP transmission coefficients are -20.7 dB and -0.5 dB, respectively, which is in good agreement with the simulations. Also, it has a bandwidth of 17.6%. This CPSS exceeds the performance described in the works of Morin (1990) and Fusco and Nair (2006).

We analyzed four variants of the CPSS based in the Pierrot cell. These variants were possible due to the flexibility of the fabrication techniques. The Pierrot cell with a load in the middle segment offered an alternative to effectively reduce the cross polarization. In comparison to the single unit cell, the loaded cell has a 15 dB reduction at the peaks of the co-pol to cross-pol ratio for the RHCP waves. The price to pay is the bandwidth which reduces to 23.3%. There is also a degradation of the RHCP transmission coefficient at high frequencies.

The next studied cell was the Pierrot cell at 90 degrees which in the end did not offer any improvements. On the contrary, the double unit cell had some interesting results. We confirmed that with two-fold rotation symmetry the cell is more independent to the variation of the angle of incidence as stated by Roy and Shafai (1996). To increase the performances even further, many cell periods were analyzed. For the double crank cell, the unit cell dimensions that gave the best results were 7 mm $\times$ 11 mm. The cell had a bandwidth of 40%. This configuration has an increased density of cells, and the improved performance resulting

from this is in line with the findings of Munk (2005) on frequency selective surfaces. A CPSS based on the double crank Pierrot cell prototype was also fabricated and characterized. The double unit cell prototype offers a bandwidth increase of 15.4% in comparison to the simple unit cell. Its performance is also less dependent on the incident angle.

To finalize the study of the double unit cell configurations, we analyzed the double cell designed for dual-frequency operation by changing the angle between the segments on one of the cells. These cells offered an excellent BW-T bandwidth greater than 40%, but the AR and the transmission coefficients for the RHCP waves were deteriorated.

We ended the study of this project with a consideration of losses in the foam layers supporting the CPSS structure. We have seen that the foam introduced most of the losses in the CPSS. To reduce them, different approaches were analyzed. A foam support with holes near the E field hot spots was fabricated. This prototype exhibited a 0.4 dB increase in the transmission coefficients for the RHCP waves. Of course the perforated structure is less rigid. This mechanical degradation might however be acceptable, depending on the application.

4.2 Limitations of the proposed solution

In this project, all the CPSS were designed to operate in the K-band. Of course, the structures can be easily scaled to work in other bands. If higher frequencies were to be chosen, one of the main factors would be the foam losses as they increase with frequency. The accuracy of the substrate folding process could also become an issue.

4.3 Future Work

The dependency on the angle of incidence was reduced using two-fold rotation symmetry. However if further improvement is desired in this direction, two dielectric layers with higher permittivity could be added to both upper and lower sides of the structure. Fig. 4.1 illustrates a CPSS with this proposed configuration. This way, and based on Snell's law, the angle of incidence θ_1 could be reduced so that the CPSS "sees" a smaller incident angle θ_2. So the whole system could work with a larger variation of the angle of incidence, thus increasing the performance of the CPSS.

In this thesis, all the considered CPSS designs had a planar support. To consider assembling a CPSS with a concave reflector shape, further study is needed to change the structure to allow more mechanical flexibility. Another approach that could be studied to make dual CP reflectors is to replace the parabolic shaped reflectors by planar reflectarrays. This would require the implementation of a phase control features in the CPSS unit cells.

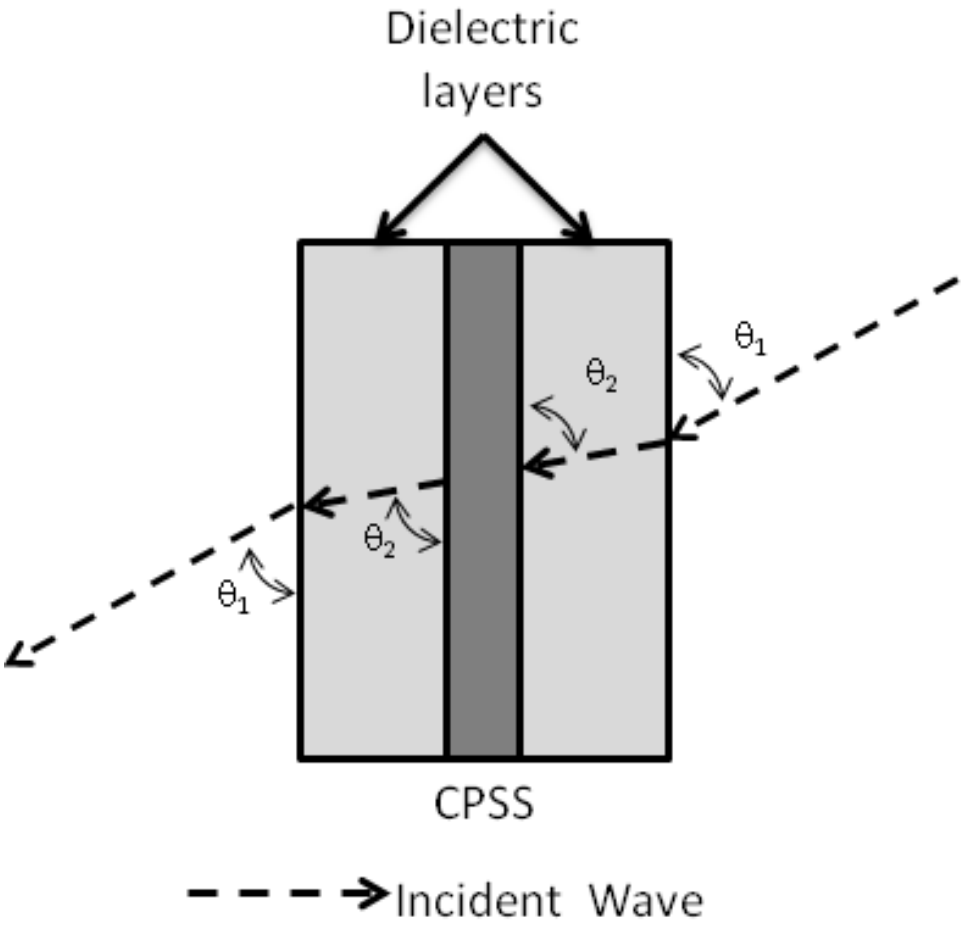

Figure 4.1: Illustration of a CPSS with dielectric layers to decrease the dependency to the angle of incidence.

REFERENCES

BHATTACHARYYA, A. (2006). *Phased Array Antennas : Floquet Analysis, Synthesis, BFNs and Active Array Systems*. Wiley Series in Microwave And Optical Engineering. John Wiley & Sons.

FUSCO, V. and NAIR, B. (2006). Circular polarisation selective surface characterisation and advanced applications. *IEE Proceedings, Microwaves, Antennas and Propagation*, 153, 247 – 252.

HOPKINS, E., HOPKINS, G. and BAILEY, C. (2010). Mechanism of apparent gain observed in focused beam measurements of a planar FSS. *Proc. 2010 IEEE Int. Symp. Antenna Propagat.* Toronto, ON, Canada, 1 –4.

JORDAN, E. and BALMAIN, K. (1968). *Electromagnetic Waves and Radiating Systems*. Prentice-Hall.

JOYAL, M. and LAURIN, J. (2012). Analysis and Design of Thin Circular Polarizers Based on Meander Lines. *IEEE Transactions on Antennas and Propagation*, 60, 3007 –3011.

JOYAL, M.-A., LAURIN, J., RIEL, M. and DEMERS, Y. (2012). A circularly polarized Dual-Gridded Reflector prototype with a meander-line circular polarizer. *Antennas and Propagation Society International Symposium (APSURSI), 2012 IEEE*. 1–2.

JOYAL, M.-A. and LAURIN, J.-J. (2011). A cascaded Circular-Polarization-Selective Surface at K band. *Proc. 2011 IEEE Int. Symp. Antenna Propagat.* Spokane, WA, USA, 2657 –2660.

MENER, S., GILLARD, R., SAULEAU, R., CHEYMOL, C. and POTIER, P. (2012). A CPSS-based reflectarray cell with reconfigurable capabilities. *2012 6th European Conference on Antennas and Propagation (EUCAP)*. Prague, Czech Republic, 808 –811.

MORIN, G. (1990). A simple circular polarization selective surface (CPSS). *Antennas and Propagation Society International Symposium, 1990. AP-S. Merging Technologies for the 90's. Digest.* Dallas, TX, USA, 100 –103 vol.1.

MORIN, G. (1995). A Circular Polarization Selective Surface Made of Resonant Helices. Report no. 1269, Defence Research Establishment Ottawa, Ottawa, Canada.

MUNK, B. (2005). *Frequency Selective Surfaces : Theory and Design*. John Wiley & Sons.

PIERROT, R. (1966). Éléments résonants en polarisation circulaire et réflecteur semi-transparent composé de ces éléments. Patten no. 89.609, 1.512.598, France.

ROY, J. (1995). *Reciprocal Circular Polarization Selective Surfaces.* PhD dissertation, Departement of Electrical and Computer Engineering, University of Manitoba, Manitoba, Canada.

ROY, J. and SHAFAI, L. (1996). Reciprocal circular-polarization-selective surface. *IEEE, Antennas and Propagation Magazine*, 38, 18 –33.

SANZ-FERNANDEZ, J., SAENZ, E., DE MAAGT, P. and MANGENOT, C. (2012). Circular polarization selective surface for dual-optics CP offset reflector antennas in Ku-band. *2012 6th European Conference on Antennas and Propagation (EUCAP).* Prague, Czech Republic, 2683 –2687.

TARN, I.-Y. and CHUNG, S.-J. (2007). A New Advance in Circular Polarization Selective Surface - A Three Layered CPSS Without Vertical Conductive Segments. *IEEE Trans. Antenna Propagat.*, 55, 460 –467.

TILSTON, W., TRALMAN, T. and KHANNA, S. (1988). A polarization selective surface for circular polarization. *Proc. 1988 IEEE Int. Symp. Antenna Propagat.* Syracuse, NY, USA, 762 –765 vol.2.

APPENDIX A

Equations for the electric fields

The equations for calculating the reflected and transmitted waves for RHCP and LHCP incident waves are given by the next equations.

$$b_1^{rR} = \frac{1}{\sqrt{2}}(S(1:1,1:1) - jS(1:1,1:2)) \tag{A.1}$$

$$b_2^{rR} = \frac{1}{\sqrt{2}}(S(1:2,1:1) - jS(1:2,1:2)) \tag{A.2}$$

$$b_1^{rL} = \frac{1}{\sqrt{2}}(S(1:1,1:1) + jS(1:1,1:2)) \tag{A.3}$$

$$b_2^{rL} = \frac{1}{\sqrt{2}}(S(1:2,1:1) + jS(1:2,1:2)) \tag{A.4}$$

$$b_1^{tR} = \frac{1}{\sqrt{2}}(S(2:1,1:1) - jS(2:1,1:2)) \tag{A.5}$$

$$b_2^{tR} = \frac{1}{\sqrt{2}}(S(2:2,1:1) - jS(2:2,1:2)) \tag{A.6}$$

$$b_1^{tL} = \frac{1}{\sqrt{2}}(S(2:1,1:1) + jS(2:1,1:2)) \tag{A.7}$$

$$b_2^{tL} = \frac{1}{\sqrt{2}}(S(2:2,1:1) + jS(2:2,1:2)) \tag{A.8}$$

The equations for the transmitted and reflected RHCP and LHCP waves when the incident waves are RHCP or LHCP are given by :

$$b_r^{tR} = \frac{1}{\sqrt{2}}(b_1^{tR} + jb_2^{tR}) \tag{A.9}$$

$$b_l^{tR} = \frac{1}{\sqrt{2}}(b_1^{tR} - jb_2^{tR}) \tag{A.10}$$

$$b_r^{rR} = \frac{1}{\sqrt{2}}(b_1^{rR} + jb_2^{rR}) \tag{A.11}$$

$$b_l^{rR} = \frac{1}{\sqrt{2}}(b_1^{rR} - jb_2^{rR}) \tag{A.12}$$

$$b_r^{tL} = \frac{1}{\sqrt{2}}(b_1^{tL} + jb_2^{tL}) \tag{A.13}$$

$$b_l^{tL} = \frac{1}{\sqrt{2}}(b_1^{tL} - jb_2^{tL}) \tag{A.14}$$

$$b_r^{rL} = \frac{1}{\sqrt{2}}(b_1^{rL} + jb_2^{rL}) \tag{A.15}$$

$$b_l^{rL} = \frac{1}{\sqrt{2}}(b_1^{rL} - jb_2^{rL}) \tag{A.16}$$